



12-2000

The study of advanced materials using neutrons

Gary W. Lynn

Follow this and additional works at: https://trace.tennessee.edu/utk_graddiss

Recommended Citation

Lynn, Gary W., "The study of advanced materials using neutrons. " PhD diss., University of Tennessee, 2000.

https://trace.tennessee.edu/utk_graddiss/8340

This Dissertation is brought to you for free and open access by the Graduate School at TRACE: Tennessee Research and Creative Exchange. It has been accepted for inclusion in Doctoral Dissertations by an authorized administrator of TRACE: Tennessee Research and Creative Exchange. For more information, please contact trace@utk.edu.

To the Graduate Council:

I am submitting herewith a dissertation written by Gary W. Lynn entitled "The study of advanced materials using neutrons." I have examined the final electronic copy of this dissertation for form and content and recommend that it be accepted in partial fulfillment of the requirements for the degree of Doctor of Philosophy, with a major in Chemistry.

Mark D. Dadmun, Major Professor

We have read this dissertation and recommend its acceptance:

Roberto S. Benson, R. J. Hinde, L. J. Magid

Accepted for the Council:

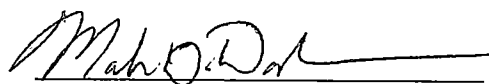
Carolyn R. Hodges

Vice Provost and Dean of the Graduate School

(Original signatures are on file with official student records.)

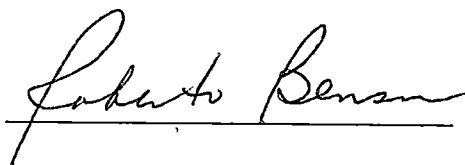
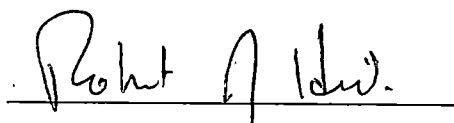
To the Graduate Council:

I am submitting herewith a dissertation written by Gary W. Lynn entitled "The Study of Advanced Materials Using Neutrons." I have examined the final copy of this dissertation for form and content and recommend that it be accepted in partial fulfillment of the requirements for the degree of Doctor of Philosophy, with a major in Chemistry.



Mark D. Dadmun, Major Professor

We have read this dissertation
and recommend its acceptance:



Accepted for the Council



Interim Vice Provost and
Dean of the Graduate School

**The Study of Advanced Materials
Using Neutrons**

A Dissertation
Presented for the
Doctor of Philosophy
Degree
The University of Tennessee, Knoxville

Gary W. Lynn

December 2000

Acknowledgments

I would like to thank Professor Mark D. Dadmun for his excellent guidance and direction, which were an impetus for accomplishing this work. A special thanks goes to Dr. Wen-li Wu, without whom none of this work would have been possible. I would like to thank Professors Roberto S. Benson, R.J. Hinde and L.J. Magid for their work as members of my committee. Much of this work was done while G.W. Lynn was a guest researcher in the Electronics Applications Group, Polymers Division, National Institute of Standards and Technology. Therefore, GWL and MDD would like to thank everyone, scientific and administrative staff, in the Electronics Applications Group, especially Eric K.Lin and William E. Wallace, for their assistance. GWL and MDD would also like to thank Steven C. Roth for his help with the evaporation of the Aluminum metal and Nathan Crawford for sharing the data in Figure 3.6.

Abstract

The first part of this thesis describes a new methodology based on a novel combination of x-ray reflectivity and small-angle neutron scattering to evaluate the structural properties of porous silica thin films about one micrometer thick supported on silicon wafer substrates. To complement these results, film composition was determined by high-energy ion scattering techniques. For the sample thin film presented here, the overall film density was found to be $(0.55 \pm 0.01) \text{ g/cm}^3$ with a pore wall density of $(1.16 \pm 0.05) \text{ g/cm}^3$ and a porosity of $(53 \pm 1) \%$. The average dimension for the pores was found to be $(65 \pm 1) \text{ \AA}$. It was determined that $(22.1 \pm 0.5) \%$ of the pores had connective paths to the free surface. The mass fraction of water absorption was $(3.0 \pm 0.5) \%$ and the coefficient of thermal expansion was $(60 \pm 20) \times 10^{-6}/^\circ\text{C}$ from room temperature to 175°C .

In the second part of this thesis, we elucidate the structure of a small molecule liquid crystal/polymer interface using specular neutron reflectivity. More specifically, we examined the interfacial transition zone width of a small molecule liquid crystal/polymer interface as a function of increasing temperature. We found that the interface between a thin film ($\approx 1000 \text{ \AA}$ thick) of the liquid crystal 4'-n-octyl-4-cyanobiphenyl (8CB) and a thin film ($\approx 800 \text{ \AA}$ thick) of deuterated poly(methyl methacrylate) (*d*-PMMA) is broad and broadens with increasing temperature. It is also observed that the thin film geometry influences the mixing behavior of the PMMA/8CB system. These results may have implications on current theories of liquid crystal display devices that are formed by the phase separation of liquid crystal polymer mixtures.

Table of Contents

Chapter		Page
1	The Study of Advanced Materials Using Neutrons.....	1
	1.1 Introduction.....	1
	1.2 Properties of Neutrons.....	2
	1.3 Examples Using Neutrons.....	3
2	Small-Angle Neutron Scattering of Nanoporous Silica Thin Films.....	14
	2.1 Introduction.....	14
	2.2 Experimental.....	22
	X-ray Reflectivity.....	22
	Small-Angle Neutron Scattering.....	23
	Ion Beam Scattering.....	25
	2.3 Results and Discussion.....	25
	Film Composition.....	25
	Overall Film Density.....	26
	Pore Wall Density and Pore Structure.....	29
	Pore Interconnectivity.....	35
	Moisture Uptake.....	38
	Coefficient of Thermal Expansion.....	39
	Conclusion.....	41
3	Neutron Reflectivity at a Small Molecule Liquid Crystal / Polymer Interface.....	45

3.1	Introduction.....	45
3.2	Experimental.....	49
	Sample Preparation.....	49
	Neutron Reflectivity.....	51
3.3	Results and Discussion.....	52
	Conclusion.....	76
	References.....	77
	Appendix.....	85
	A.1 Small-Angle Neutron Scattering.....	86
	A.2 Neutron Reflectivity.....	96
	Vita.....	107

List of Figures

Figure		Page
2.1	Cross section of a typical VLSI multilevel interconnect system...	15
2.2	X-ray reflectivity result for the sample.....	27
2.3	Schematic depicting the correlation length, average dimension of pores and pore wall material.....	31
2.4	Debye plot for the sample in air.....	34
2.5	Debye plot for the sample in <i>d</i> -toluene.....	37
2.6	Debye plot for the sample immersed in D ₂ O.....	40
2.7	Fourier transform of the reflectivity fringes.....	42
2.8	Film thickness vs. Temperature.....	43
3.1	Depiction of the various thin films and their arrangement on the silicon substrate (not drawn to scale).....	50
3.2	Neutron reflectivity data measured consecutively at 75 °C.....	53
3.3	Neutron reflectivity data measured at (25, 50, 75 and 110) °C.....	54
3.4	Magnified view of region $0.02 \leq Q_z \leq 0.07$	55
3.5	Neutron reflectivity data and best fit for the system at 25 °C.....	57
3.6	Relative scattering length density as a function of the layer depth (z) for the sample at 25 °C.....	60

3.7	Bulk 8CB/PMMA phase diagram as determined by optical microscopy.....	62
3.8	Breadth of the 8CB/ <i>d</i> -PMMA interface as a function of temperature.....	64
3.9	8CB and <i>d</i> -PMMA are completely miscible to form a single phase.....	67
3.10	8CB is energetically preferred by both the aluminum and silicon surfaces.....	68
3.11	<i>d</i> -PMMA is energetically preferred by both the aluminum and silicon surfaces.....	69
3.12	8CB prefers aluminum surface only.....	70
3.13	<i>d</i> -PMMA prefers aluminum surface only.....	71
3.14	Schematic of a liquid crystal in contact with a solid substrate.....	74
A.1.1	Initial, scattered and resultant wave.....	87
A.1.2	Illustration of the differential scattering cross section.....	88
A.2.1	Relationship between reflected and refracted radiation.....	98
A.2.2	Medium with thickness <i>d</i> , on a substrate.....	101
A.2.3	Reflectivity profile of PMMA on a silicon substrate.....	103

Chapter 1

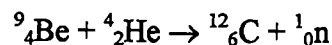
The Study of Advanced Materials Using Neutrons

The purpose of this chapter is to give the reader a brief introduction into one of nature's most fundamental particles, the neutron. The introduction includes historical and background information. Some specific examples of how neutrons are used to study the structure of matter are also discussed. Most important, the question of why one should use neutrons as an experimental tool is answered.

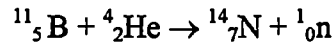
1.1

Introduction

The discovery of neutrons is credited to James Chadwick of Cambridge [1], who in 1932 observed a penetrating radiation composed of particles of finite mass and no electric charge. Bothe and Becker also observed this radiation in 1930, but it was Chadwick who elucidated its nature [2]. Irene Curie and Frederic Joliot also observed the same penetrating radiation in 1932 [3], but they believed the radiation to be high-energy gamma particles, at that time the only known uncharged radiation. Curie and Joliot were the first to observe that when it passed through a hydrogenous media, this radiation created recoiled protons that could be detected in an ionization chamber. Chadwick proved that the energies of the recoil protons were of such a value that the radiation must be composed of particles with masses comparable to protons, and called them neutrons. In these experiments, neutrons were produced in nuclear reactions when boron or beryllium nuclei were bombarded by alpha particles.



and



From these reaction schemes it is evident that the neutrons must be fundamental particles of a nucleus because the loss of a neutron changes its mass. Earlier attempts were also made by Lord Ernest Rutherford to describe this type of behavior [4]. Lord Rutherford had speculated that these interactions were due to the formation of a neutral bound pair containing a proton and electron and that this bound pair resided in the nuclei. This model turned out to be wrong. Later it was shown that the de Broglie wavelength of electrons is so much larger than nuclear dimensions that this light particle can not reside in a nucleus. Despite the fact that Rutherford's model was wrong, he did correctly predict some properties of neutrons.

1.2

Properties of Neutrons

The mass of a neutron is 1.675×10^{-27} kg, while the de Broglie wavelength of neutrons is on the order of interatomic distances in solids and liquids. This implies that interference effects between scattered neutrons can occur which yield information on the structure of the scattering system. This property of neutrons is addressed and further detail is given in Appendix A of this thesis. The neutron has a charge of zero, which means not only that it can penetrate deeply into a sample, but also that it comes close to the nuclei because there is no Coulombic barrier. This means that neutrons can be scattered by nuclear forces, more specifically via the strong nuclear force. Some nuclides do scatter neutrons more strongly than others do. The interaction of neutrons with nuclei varies randomly with

atomic number [5]. The strength of this interaction is characterized by a parameter known as the scattering length. Hydrogen and one of its isotopes, deuterium, have very different scattering lengths. Because of this difference, molecules can be labeled by substituting hydrogen for deuterium, which essentially highlights certain molecules or parts of molecules. However, one must be careful and remember that the thermodynamics of the system may change after the chemical substitution of deuterium for hydrogen. High labeling concentrations coupled with high molecular weights may cause phase separation in polymer blends. A polymer that is labeled with deuterium has a greater excluded volume; also smaller entropy of mixing results and the polymers can phase separate [55]. Neutrons also have a magnetic dipole moment ($\mu_n = -1.913 \mu_N$) with spin of $\frac{1}{2}$ [5], which means that neutrons can interact with unpaired electrons via magnetic forces. Therefore neutrons can interact with matter in one of two ways, either with nuclei via the strong nuclear force or with unpaired electrons via the magnetic force. Now that some of the historical background and the fundamental interactions of neutrons have been discussed, the rest of this chapter is devoted to providing examples of how neutrons can be used to probe matter.

1.3

Examples Using Neutrons

The ability to characterize ultra-thin polymer films at interfaces and surfaces is important to a large number of industrial applications. Electronic packaging, dielectric layers, coatings, composites, lubrication and biocompatible materials are just a few of these applications [6]. For example, in a composite material, if there is poor adhesion

between the polymer and filler material or if the polymer does not wet the filler material, the desired properties of the composite can not be obtained. In order for polymers to be used in biocompatible applications such as implants, the material must retain mechanical strength and at the same time, the surface must be compatible with human tissue.

It is usually the interfacial behavior of an ultra-thin polymer film that determines its end use in microelectronics [7]. In applications for microelectronics, multiple layers of polymeric materials are typically used. If these multiple layers consist of different polymers, the individual layers must adhere to each other, or peeling would occur and multi-layering would not be possible. Thermal stability is also a major issue for ultra-thin polymer films in microelectronics since processing involves large thermal variations and cycling. For instance, does the glass transition temperature of polymer thin films differ from polymers in the bulk? This is one unresolved problem that exists in the physics of polymer interfaces. An important question then becomes: what techniques can one use to elucidate the structure and physics of polymer interfaces?

Numerous techniques have been used to examine the interface and surface behavior of polymers. Optical methods such as ellipsometry [8] and second harmonic generation (SHG) [9,10] have been used. One advantage of optical methods is that they are readily available and can be assembled on a lab bench top. However, there are two major disadvantages: a.) The wavelength of visible light is on the order of several hundreds of nanometers (nm) so one can only resolve spatial resolutions down to several tenths of a micron (μm), b.) In a multi-component system, there must be sufficient difference in the refractive indices of the individual components to provide sufficient contrast.

Ion-beam techniques that include Rutherford back-scattering spectrometry (RBS) [11,12], forward recoil elastic spectrometry (FRES) [13-15] and secondary ion mass spectrometry (SIMS) [16-18] are also useful to investigate polymer interfaces. These ion beam methods can measure the polymer composition profile normal to the surface with spatial resolutions down to 10 nm. A disadvantage to these methods is that the ion beam degrades the samples. Thus one must use several samples to study kinetic behavior of a particular system. Ion beam experiments are also carried out in high vacuum, which precludes the use of liquid samples. Despite these drawbacks, advances have been made in understanding the adhesion [19] and diffusion [11-15] of polymers and the ordering of thin films of block copolymers [16,17] using ion beam techniques.

Transmission electron microscopy (TEM) [20,21] can image a thin film polymer surface down to 1 nm. It has been used to study the effects of surfaces on thin films of block copolymers. But again, there are some drawbacks to the procedure. Sample preparation can be difficult in that the thin film must be stained in order to provide sufficient contrast. Like the ion beam methods, the sample may be damaged by the beam during the experiment. Benefits include the fact that detail in thin films can be seen with excellent depth resolution to depths of well over 100nm, and the direct observation of morphologies is possible.

X-ray photoelectron spectroscopy (XPS), an important tool for surface science, can also determine the thin film polymer composition profile at the vacuum / sample interface. XPS can penetrate polymer sample surfaces down to 7nm with a spatial resolution of 0.1nm [22-25]. Again, a major disadvantage is that the X-ray beam destroys the sample

so that repetitive measurements cannot be made on the same sample.

A promising technique to study polymer surfaces and buried interfaces is neutron reflectivity. Neutron reflectivity can be considered a subset of small-angle neutron scattering. Specular reflectivity is the special condition when the angle of detection is equal to the angle of incident neutrons. This technique is superior to optical methods and ion beam techniques in measuring properties of thin films, and can yield information on variation in composition normal to a surface. Unlike other measurement techniques such as ion-beam scattering, neutron reflectivity is a nondestructive probe; therefore repetitive measurements can be made on the same sample. Other advantages include a spatial resolution down to 10 angstroms (\AA) and a penetration depth of more than 1000 \AA [26]. Examples of parameters that can be determined by neutron reflectivity include overall thickness of a thin film and the thickness of individual layers if the thin film consists of multiple layers [26]. The interfacial and surface roughness of the thin film can also be measured, where the interfacial roughness is the gradient in the density between consecutive layers [26]. The variation in neutron scattering length density normal to the surface is the quantity that is determined in neutron reflectivity. Contrast in a multi-component system can therefore be obtained by selective deuteration of an individual component. Based on these attributes, neutron reflectivity has clearly many advantages when it comes to investigating thin polymer films. To support this claim, it is best to look at a few examples.

Neutron reflectivity is well suited for studying the interdiffusion of two thin film polymers. Stamm *et al.* studied two thin poly(styrene) (PS) films on a glass substrate in

which the lower film was protonated and the upper film was deuterated [27,28] to yield a pronounced contrast in the scattering length density. The contrast would be zero for the case of X-rays. They observed that after annealing at 120 °C, the scattering length density profile is changed due to interdiffusion of the polymers at the protonated polymer / deuterated polymer interface. Protonated polymer chains at the interface do not hinder the mobility of deuterated chain segments for short annealing times. They observed that the reflectivity is only changed at larger wavevector transfers and attributes this to the fact that only the relatively short chain lengths are involved in a random walk type of movement. After very long annealing times, whole-deuterated chains start to move into channels, which are formed from the diffusion of the protonated chains. This reptation behavior predicts that the reflectivity will be changed for smaller wavevector transfers, and this is exactly what was observed by Stamm *et al.*

Wu *et al.* have used neutron reflectivity to measure the density profiles of poly(methyl methacrylate) (PMMA) thin films on silicon (111) single crystal wafers [29]. They found a 45Å thick layer at the free polymer surface that has a density about half the value of bulk PMMA for a film with a total thickness of 700Å. After heating above the glass transition temperature, the diffuse layer disappeared and the thin film density profile was transformed to one with a sharp free polymer surface. This is a prime example of how reflectivity can measure the composition of thin films normal to the surface.

Wallace *et al.* studied the thermal expansion of poly(styrene) (PS) thin films supported on hydrogen terminated silicon substrates using reflectivity [30]. They observed that films on the order of 400 Å and thinner show no glass transition temperature up to at least 60

°C (160 °C), above the bulk transition temperature of 100 °C. They used reflectivity to measure the thickness of the films while increasing the temperature of the sample. A break in the thickness versus temperature curve signals the glass transition and the onset of bulk behavior, which was observed in films thicker than 400 Å. Orts *et al.* have also studied thin films of PS using reflectivity [91]. Measuring the thickness versus temperature for PS thin films around 400 Å supported on silicon with a native oxide surface, they saw the glass transition temperature decrease by as much as 30 °C. These two experiments illustrate the importance that the character of the interface between a polymer and solid substrate has on the glass transition temperature of the polymer. These two experiments also show the importance of measuring spatial resolution on thin film thickness and that reflectivity is the best technique for doing so. Can neutron reflectivity be used to study other thin film materials besides polymers?

Neutron reflectivity is also a powerful tool for studying thin films of liquid crystals. Olbrich *et al.* used reflectivity to investigate the smectic order and the smectic-A to smectic-C* phase transition thin films of a chiral ferroelectric liquid crystal mixture [31,32]. The liquid crystal thin films were between 150 and 600 Å thick. They demonstrated that it is possible to extract the tilt angle in ferroelectric liquid crystals from reflectivity measurements of thin films. The authors went on to show that smectic-A to smectic-C* phase transition temperature and the temperature dependence of the tilt angle in the smectic-C* phase are almost independent of the film thickness down to 200 Å and are similar to those in the bulk.

Phillips *et al.* using neutron reflectivity [33] studied the porosity and surface roughness

of three different liquid crystal alignment layers. The authors used a contrast variation method by measuring the scattering length density profile of absorbed hexane into alignment layers of liquid crystal. Two different surfaces were used to align the liquid crystals, a rubbed polyimide surface and a silicon oxide surface. They observed that the alignment layers of the liquid crystal were smooth and impervious to hexane for the polyimide surface. The silicon oxide surface produced a rough and porous character for the liquid crystal alignment layers.

By this point, I believe the importance of neutron reflectivity is evident. Neutron reflectivity is a superior method for characterizing thin film materials, including not only polymer thin films, but also liquid crystal thin films. Phenomena such as polymer diffusion, the glass transition temperature and density profile in polymer thin films and phase transitions and alignment of liquid crystal thin films are readily observed using neutron reflectivity. However, neutron reflectivity is just one of many experimental techniques that uses neutrons.

Small-angle neutron scattering is another method which uses neutrons. In general, small-angle scattering is used to study the structure of matter. As was mentioned earlier in section 1.2, it is the de Broglie wavelength of neutrons, which is on the order of interatomic distances, that leads neutrons to be useful in studying the structure of matter. Neutrons can scatter in one of several ways. The type of neutron scattering depends on the incident wave frequency and the scattered wave frequency. The scattering event itself may or may not involve an energy change. If there is no change in energy upon scattering, then the scattering is elastic. Inelastic scattering occurs when there is a change in the

energy of the scattering event. The total scattering signal constitutes both coherent and incoherent scattering. Coherent scattering contributions are from structural spatial correlations between scattering centers. If the scattering centers are randomly distributed with no set correlation, then the scattering is incoherent. In this manuscript, it is relevant to discuss coherent elastic scattering of neutrons. Coherent elastic scattering of neutrons measures the correlations of scattering centers within a medium providing information about the structure. A more detailed analysis of small-angle neutron scattering is given in chapter 2. Why is the structure of matter so important?

In polymer science, the structure of polymers in various environments is an extremely important topic. The size and shape of polymers in solution determine their viscosity, which is a key property in processing [34]. The degree of crystallinity in polymer fibers determines their end use applications [34]. The structure of polymers under a shearing force can predict complications or the ease of melt extruding [34]. Structural biology is one of the most important fields in the life sciences. Hydrogen atoms and water molecules around DNA and proteins play an important role in many physiological functions [35]. It is the size and surface area of pores in porous media that leads these media to be useful in certain chemical separation processes [36]. For the remainder of this chapter, some specific examples of small-angle neutron scattering will be given.

For a long time, the experimental determination of the conformation of a linear polymer chain in its melt was unsolved [37]. It was first thought that the polymer chains were one of three different conformations: the chains are randomly interpenetrated and each one adopts a random coil conformation, the chains are collapsed onto themselves or

the chains are partially aligned in a way similar to that of crystalline polymers. Due to their incompressibility, homogenous polymer melts do not readily scatter radiation; basically, contrast does not exist. However, if one or a few of the chains could be labeled in such a way as to distinguish them from the rest, one should observe a scattering pattern. The labeling method for light or X-rays scattering involves a mixture of polymers of different chemical species. But labeling chains in this way usually results in phase separation of the polymer mixture. Thus, the only feasible solution is isotopic substitution, which is used in small-angle neutron scattering. Lieser *et al.* [38] used this isotopic labeling technique to look at poly(styrene) in the melt while Wignall *et al.* [39], Kirste *et al.* [40] and Cotton *et al.* [41] used the same method to study poly(methyl methacrylate) and poly(ethylene). They all found that the values for the radius of gyration of the chain vary as it would for a chain in its theta solvent. A polymer chain in its theta solvent assumes an unperturbed chain dimension and is recognized to be ideal. Thus in a melt, polymer chains are ideal. This is a consequence of a balance between intermolecular and intramolecular interactions, which was predicted by Flory [42]. Flory predicted that a polymer chain in the melt should be ideal, however, it was not until the advent of using neutrons in small-angle scattering that Flory could be proved or disproved.

Scattering may be used to study the thermodynamics of polymers in solution. In particular, the second virial coefficient can be measured. The second virial coefficient is related to the Flory-Huggins interaction parameter χ . The interaction parameter is the difference in energy between a solvent molecule when it is immersed in pure polymer and when in pure solvent. Light scattering techniques are able to measure the second virial

coefficient, however, the advantage in using small-angle neutron scattering is that it is possible to measure the second virial coefficient in semidilute and concentrated polymer solutions. Cotton *et al.* were able to measure the second virial coefficient and the screening length for semidilute solutions of poly(styrene) in deuterated hexane [43]. The screening length is the maximum distance between two monomers for which significant interactions exist between them. At distances greater than the screening length, the excluded volume has no influence and the chain behaves like a Gaussian chain.

Small-angle neutron scattering can also be used to measure the structure in two and three phase systems. Wignall *et al.* were able to elucidate the structure and volume composition in carbon black filled poly(ethylene) composite materials using small-angle neutron scattering [44]. Carbon black is often used as a filler material to modify the electrical and mechanical properties of polymers. The end use properties of the polymer composite depend on the size and shape of the carbon black particles. It is an advantage if one could know the size of carbon black agglomerates and volume fraction in the composite material.

A brief historical background and discussion of the fundamental properties of neutrons has been given. The advantages of neutrons for probing matter have also been addressed. Two specific techniques in neutron science, neutron reflectivity and small-angle neutron scattering have been given as examples for what one might use. As one can see, there are many applications for which neutrons are best suited. In chapter two, a more detailed explanation of small-angle neutron scattering will be discussed and how we used it to determine the structure of nanoporous silica thin films. The technique of neutron

reflectivity is discussed in chapter three and how it was used to probe the interface between a small molecule liquid crystal and a polymer.

Chapter 2

Small-Angle Neutron Scattering of Nanoporous Silica Thin Films

Included in this chapter is a description of how we used neutrons in combination with ion beam scattering and X-ray reflectivity as analytical tools to characterize spin-on nanoporous silica thin films. Section 2.1 is an introduction and outline for our motivation followed by the experimental set up in section 2.2. A discussion of our results is given in section 2.3. The work in chapter two is a project developed in conjunction with Dr. Wenli Wu, leader of the Electronics Applications Group, Polymers Division at the National Institute of Standards and Technologies.

2.1

Introduction

Increasing microprocessor performance is a field of study that has gained much importance in science and technology. In order to continue improvement of microprocessor performance, it is necessary to decrease the size of the very-large-scale-integrated circuits (VLSI) that make up a microprocessor chip. These circuits are used to build up application-specific-integrated circuits (ASIC). These ASIC act as functional blocks, such as cache control, within the microprocessor chip. Decreasing the size of the VLSI allows for faster microprocessor chips, an increase in the number of functions of a single chip and an increase in packing density of the VLSI. In addition, VLSI can be arranged in a multilevel structure so that the area of the silicon wafer, on which the circuits are produced, can be preserved. Figure 2.1 is a schematic diagram of the cross section of a typical VLSI multilevel interconnect system. As one can see, this system is

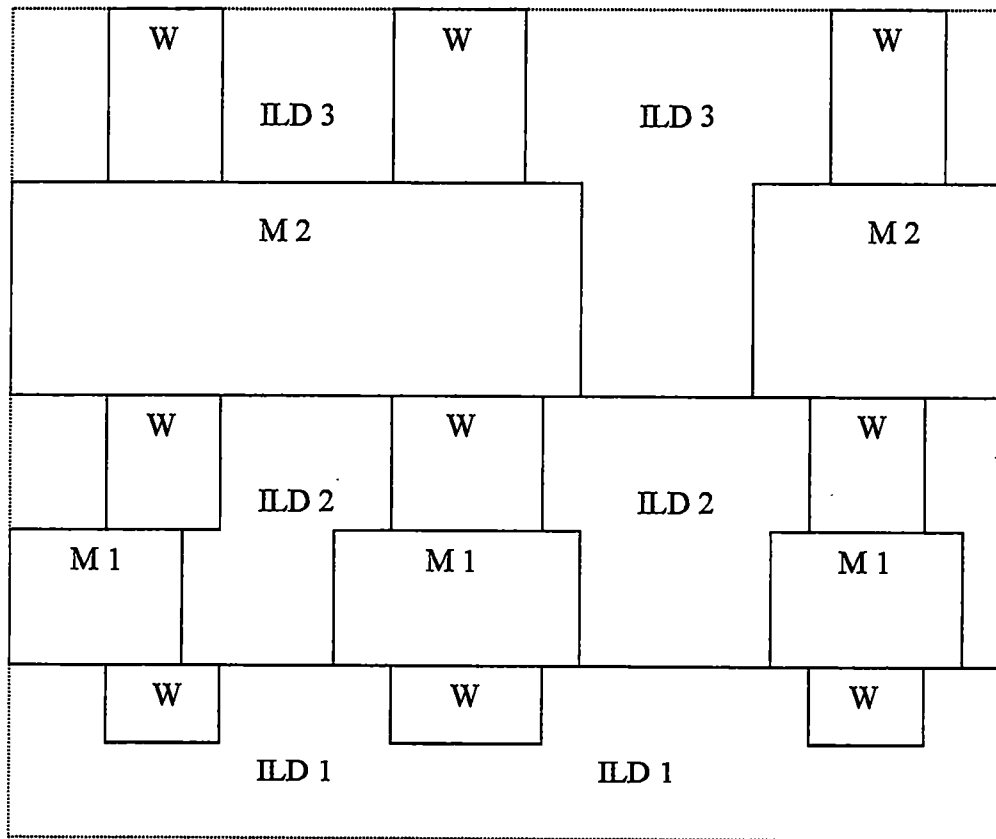


Figure 2.1. Cross section of a typical VLSI multilevel interconnect system

made from various numbered layers composed of metal interconnects (M), separated by an interlevel dielectric material (ILD), and tungsten contacts (W). The interlevel dielectric material serves as an insulator to isolate the current in the metal interconnects. By decreasing the size of the VLSI, the distance that the current must travel through the metal interconnect lines is decreased, therefore increasing the speed of the device. However, complications arise with an increase in packing density of the VLSI. The number of interconnects is increased, which in turn increases the capacitance between the interconnect lines. Undesired effects from an increased capacitance include propagation delay and crosstalk noise. Although decreasing the size will improve the speed and performance, the problem of increasing capacitance between interconnects limits the current technology. In order to get past this limitation, new materials must be designed for interlevel dielectric materials (ILD) in VLSI that provide the insulation properties.

New materials that are to be designed for ILD applications must meet stringent requirements. An exacting combination of electrical, thermal, mechanical and chemical properties must be met (see Table 2.1) [45]. These properties must also be accomplished at a submicron length scale and remain uniform over the entire area of the device. In order to keep up with an increasing packing density of VLSI, the ILD material must have a dielectric constant (k) of 2 or less. Another material requirement of ILD is a low coefficient of thermal expansion (CTE) in order to prevent fractures in VLSI. Aluminum alloys are typically used as the metal interconnects. VLSI are processed at high temperatures and if the ILD material expands faster than the aluminum alloy, the device can fracture. Low moisture absorption is another important factor when designing these ILD materials. The various levels in VLSI (See Figure 2.1) are typically planarized in a

Table 2.1. Necessary material properties for ILD applications

Electrical	Thermal	Chemical	Mechanical
Dielectric constant less than 2	High thermal stability	Chemical resistance	Thickness uniformity
Low charge trapping	High thermal conductivity	Low moisture absorption	Good adhesion
Low leakage current	Low coefficient of thermal expansion	High purity	Crack resistance
High reliability	Low thermal shrinkage	Long storage life	Low stress

chemical-mechanical polishing (CMP) slurry. During the CMP process, the ILD material is exposed to water. Even the smallest amount of moisture absorbed by the ILD material can cause the VLSI to short.

Leading candidates for next-generation low-dielectric-constant material to be used in ILD applications are porous silica thin films [46]. The dielectric constant for pure silica is around 4. The dielectric constant for air is 1. The introduction of pores or voids will thus lower the dielectric constant of the base silica material. When the film porosity reaches three-quarters by volume, the dielectric constant can effectively be lowered to 2 [47]. This lowered dielectric constant has the effect of increasing signal propagation speed, decreasing the minimum energy needed to propagate a signal and decreasing the crosstalk between adjacent conductors. Another advantage to using porous silica thin films as interlevel dielectric material is that industry already has the process conditions in place for using silicon. Switching over to new silica based technologies would be an economical and easy transition. A major disadvantage in using porous silica films for ILD materials is that a high degree of porosity causes the films to have low mechanical strength. CMP processing can break apart the films if they are too porous. However, by optimizing the porosity, one can achieve the necessary balance between a low dielectric constant, moisture absorption, CTE, and high strength.

There exist numerous techniques to characterize the performance properties of interlevel dielectric thin films such as X-ray photoelectron spectroscopy (XPS) [48]. XPS can determine the composition profile at a vacuum / sample interface and give an estimate of the pore density. However, few techniques exist to measure structural properties such as porosity and pore size of porous films less than 1 micron thick. As one

might guess, the porosity and pore size are intimately related to the performance of the material. Armed with *a priori* knowledge of porosity and pore size, the chemical composition and processing conditions could be varied to achieve the desired performance properties. In order to advance the technology, suitable measurement techniques must be developed to characterize these porous silica thin films.

The purpose of this work is to develop a methodology to characterize porous thin films which are about 1 micron thick and supported on silicon wafers. The porous thin films are generally too fragile to remove from the silicon substrate, so the characterization must be accomplished while the films remain adhered to the substrate. Additionally, these porous thin films are usually processed on the substrate and their properties may differ from that in the bulk state. Therefore, it is important to characterize these thin films while attached to the silicon substrate. The structural properties to be measured include the overall film density, pore-wall density, porosity, average pore size, and pore connectivity. The parameters of overall film density, pore-wall density, porosity and average pore size are important for correlating observed thermomechanical behavior with structure so that improvements in material selection and/or material processing may be optimized. The parameter of pore connectivity is important in cases when the thin films are exposed to wet environments such as in chemical-mechanical polishing processes. In theory, a thin film that has pores connected to the surface may result in an uncontrolled increase in the dielectric constant or leakage current due to penetration of contaminant materials such as water or chemicals from the polishing process. In addition to the structural properties to be measured, the out of plane coefficient of thermal expansion (CTE) will be determined. As was mentioned earlier,

the CTE is an important material parameter. If a mismatch exists between the CTEs of the ILD material and the metal interconnect fracture in the VLSI can occur.

The key measurement techniques used in this work are specular X-ray reflectivity [52-54] and small-angle neutron scattering (SANS) [55]. Reflectivity will be discussed in detail in chapter three, and SANS will be discussed in detail in section 2.3. The novelty of this work is based on the use of a new high resolution X-ray reflectometer to accurately measure film thicknesses greater than one micron, and the treatment of complementary data obtained from both X-ray reflectivity and SANS as a set of simultaneous equations to quantitatively determine the structural parameters of the porous thin films. The methodology and results for a 900nm thick porous silica (xerogel) thin film test sample, Allied Signal Nanoglass™ K2.2-A10B, will be reported to exemplify the technique which was then used to also characterize 20 porous silica thin films provided by E. Todd Ryan and Huei-Min Ho at International Semiconductor Manufacturing Technology (SEMATECH). The Nanoglass sample was prepared by spin coating on silicon wafer (8-inch diameter, 1/16-inch thick) using sol-gel methods.

For this work, we used the simplest description of a porous material; a two-phase model where one phase comprises the voids and the connecting material is the other phase. The connecting material between the voids, i.e. the pore wall material, is assumed to have a uniform density. Assuming uniform density results in two unknowns, the porosity, P , which is the volume percentage of the pores, and the pore wall density, ρ_w . These two variables cannot be solved from either X-ray reflectivity or SANS data alone. Therefore, we performed both measurements on the same sample. By solving two equations involving the variables P and ρ_w , the values of P and ρ_w can be determined. In

order to solve these two equations simultaneously, we must also know the thin film chemical composition. Thin film chemical composition was measured using a combination of Rutherford backscattering spectrometry (RBS) for silicon, oxygen, carbon, and forward recoil elastic scattering (FRES) for hydrogen. The thin film chemical composition is used to convert the electron density to mass density in the X-ray reflectivity data analysis, and to determine the scattering contrast between the pore wall material and pores in the SANS analysis.

Questions of pore connectivity and moisture uptake are addressed by conducting SANS measurements on the sample immersed in either a deuterated organic solvent or deuterated water. If the sample has channels that are connected to the surface, solvents with low interfacial tension can readily fill and wet these pores. Deuterated toluene is such a solvent and spreads readily on the surfaces of all samples tested. The contact angle measured was usually less than 5° . Deuterated water was found to have a much higher contact angle, typically around 90° , and consequently not found to fill the pores of the sample. If the pores are filled with a deuterated solvent, the scattering contrast changes notably depending on the neutron scattering length of the deuterated solvent used. The percentage of the pores filled by solvent or water is, therefore, estimated from the difference in SANS intensity between thin films before and after immersion.

The out of plane coefficient of thermal expansion normal to the sample surface is calculated using film thickness information from the spacing of the interference fringes in the X-ray reflectivity data as a function of temperature.

2.2

Experimental

X-ray Reflectivity

At an X-ray wavelength of a few tenths of a nanometer, the refractive index of most materials is less than one. Hence, there exists a critical angle below which total external reflection of the radiation occurs. This critical angle, θ_c , can be approximated by $(\rho r_e \lambda^2 / \pi)^{1/2}$, where ρ is the electron density or the number of electrons per unit volume of the material, r_e is the classical electron radius which is equal to 2.818 fm, and λ is the X-ray wavelength. All the angles used within the context of X-ray reflectivity are defined as grazing angles measured from the surface parallel. At an incident angle below θ_c , total reflection occurs. In a typical X-ray reflectivity measurement, the reflected intensity is collected as a function of the incident angle as it is continuously varied through the critical angle. By modeling the reflectivity result with a one-dimension Schrödinger equation, the details of the electron density profile normal to the surface can be deduced [58]. Free-surface roughness, interfacial roughness and density variations in the thickness direction of the sample can also be determined by using computer modeling procedures to create electron density depth profiles that best fit the experimental data. The information reported here from the X-ray reflectivity is an average over a lateral dimension of a few micrometers as dictated by the coherence length of the X-ray beam.

The X-ray reflectivity results are specular data collected with the grazing incident angle equal to the detector angle. The angle ranged from 0.05° to 0.6° . The X-ray reflectivity measurements were conducted in a θ - 2θ configuration with a fine-focus copper X-ray tube. The incident beam was conditioned with a four-bounce germanium

[220] mono-chromator. The beam was further conditioned with a three-bounce germanium [220] channel cut crystal situated before the detector. This configuration results in a copper $K_{\alpha 1}$ beam with a fractional wavelength spread, $\Delta\lambda/\lambda$, of 1.3×10^{-4} and an angular divergence of 12 arcsec. A closed-loop active servomechanism controls motion of the goniometer with an angular reproducibility of 0.0001° . Without these high precision settings in both the X-ray optics and the goniometer control, it would be impossible to detect the very narrowly spaced interference fringes from films on the order of 1 micron thick. Thus, it would not be possible to determine accurately the thickness of the thin films.

Small-Angle Neutron Scattering

The SANS measurements were conducted on the NG1 8-Meter instrument at the National Center for Neutron Research at the National Institute of Standards and Technology. Scattering was performed on thin film samples with the beam incident along the surface normal. A wavelength, λ , of 6 Å was used with a wavelength spread, $\Delta\lambda/\lambda$, of 0.25. A distance of 3.6 meters was the sample to detector distance. The detector was offset by 3.5° from the incident beam in order to increase the observed angular range. The resultant scattering vector, q (where $q = (4\pi/\lambda) \sin(\theta/2)$ and θ is the scattering angle from the incident beam path), ranged from 0.01 to 0.18 \AA^{-1} . The SANS results and the structural parameters deduced from them are quantities averaged over the scattering volume of approximately $1 \text{ cm}^2 \times 5 \text{ }\mu\text{m}$. The sample was prepared by cleaving the silicon wafer with the thin film attached into 4mm x 1mm pieces. These pieces were then stacked, six or more at a time, in a rectangular quartz cell. In this way, the signal from the scattering intensity may be enhanced. This is a well-documented method for the

study of thin films on silicon substrates by SANS [59]. The scattering intensities in the small-angle region (less than 5°) are exclusively from the porous thin film. The silicon wafers themselves are practically transparent to neutrons and the wafer does not cause any scattering in this small-angle region, as verified by measurement of the scattering from a stack of six bare silicon wafers. Two-dimensional scattering intensity data were collected from each thin film sample stack and were corrected for the empty quartz cell scattering, background counts, detector uniformity and sample thickness. The scattering intensity data were reduced to an absolute scale by using a 1.0-mm thick water sample as a standard. The two-dimensional data were circularly averaged to produce one-dimensional scattering intensity profiles. The scattering length contrast arises from the difference in the neutron scattering of the connecting pore wall material and the pores themselves. The neutron scattering length of the pores or voids is taken to be zero.

For the porous thin films studied, three different SANS samples were prepared; one in air, one with the sample immersed in deuterated toluene (*d*-toluene) and one with the sample in deuterated water (D_2O). Samples were immersed in the solvents for at least 24 hours prior to measurement. All of the SANS measurements were conducted at room temperature and atmospheric pressure. SANS results for the samples in air are used in conjunction with the X-ray reflectivity results in order to determine wall material density, ρ_w , porosity, P , and the size of the pores, as was previously discussed. SANS results from the *d*-toluene immersed samples were analyzed to determine the pore connectivity. The moisture uptake of the samples was determined from the SANS results of the sample in D_2O .

Ion Beam Scattering

High-energy ion beam scattering techniques were used to determine the chemical composition of the thin film samples [60]. Professor Russ Composto and Howard Wang performed the ion scattering work reported here at the Surface and Thin Film Analysis Facility at the University of Pennsylvania, Philadelphia. A mono-energetic beam of α particles is directed toward the thin film sample held in a vacuum. The scattered energy of the α particles is proportional to the mass of each target species. In our case the target atoms are silicon, oxygen, and carbon atoms. By detecting the relative number of scattered α particles as a function of energy, and applying the well-known scattering cross-section for each element, direct integration or computer modeling of the scattering peaks gives the relative abundance of each element. This technique is generally termed Rutherford backscattering spectrometry (RBS). Hydrogen will not show a backscattering peak since it is lighter than the α particles used. Instead, it is forward recoiled upon impact with an incoming α particle. By directing the α particle beam at grazing incidence to the sample surface, in this case 15° , hydrogen atoms in the sample can be forward recoiled to a detector. Chemical composition analysis is performed in the same way as with RBS. This technique is termed forward recoil elastic scattering (FRES) or elastic recoil detection (ERD).

2.3

Results and Discussion

Film Composition

The first task in analyzing the ion beam scattering data was to subtract out the silicon substrate. In order to do this, the beam was held at a grazing incidence angle of 15° from

the sample surface with an α particle beam energy of 1.8 MeV. After identifying the plateau due to the substrate, the substrate background was subtracted out using a spline fit. The sample was then positioned normal to the beam with an energy of 3.4 MeV. A RBS spectrum was collected and the data fitted to determine the amount of carbon, oxygen and silicon in the thin film. FRES was then used to measure the amount of hydrogen in the porous thin film. From direct peak integration of the FRES signal, the thin film was found to contain 33 % hydrogen. The RBS signals were computer modeled to reveal a thin film composition of 19 % silicon, 34 % oxygen and 14 % carbon. The detection limit is on the order of 5% for each element.

Overall Film Density

Figure 2.2 shows the X-ray reflectivity results for the Nanoglass sample. The dashed line indicates the data while the solid line is the best fit to the data. The results are presented as the logarithm of the ratio of the reflected beam intensity, I_r , to the incident beam intensity, I_0 , versus Q_z . Q_z is the magnitude of X-ray momentum transfer normal to the sample surface and is defined as $(4\pi/\lambda) \sin\theta$ (where λ is the copper $K_{\alpha 1}$ wavelength of 0.15406nm and θ is the grazing incidence angle). Inspection of Figure 2.2 shows that there are two critical angles, one at $Q_z = (0.0155 \pm 0.0003) \text{ \AA}^{-1}$ and the other at $Q_z = (0.0320 \pm 0.0006) \text{ \AA}^{-1}$. The critical angle at $Q_z = 0.0155 \text{ \AA}^{-1}$ is attributed to the porous silica thin film and the position can be related to the mean electron density of the film. The critical angle at $Q_z = 0.0320 \text{ \AA}^{-1}$ corresponds to that of the silicon wafer. Q_z is equal to $(4\pi/\lambda) \sin\theta$, so using $Q_z = 0.0155 \text{ \AA}^{-1}$, one determines θ , which is the critical angle for the porous silica thin film. Once the critical angle is known, the electron density is

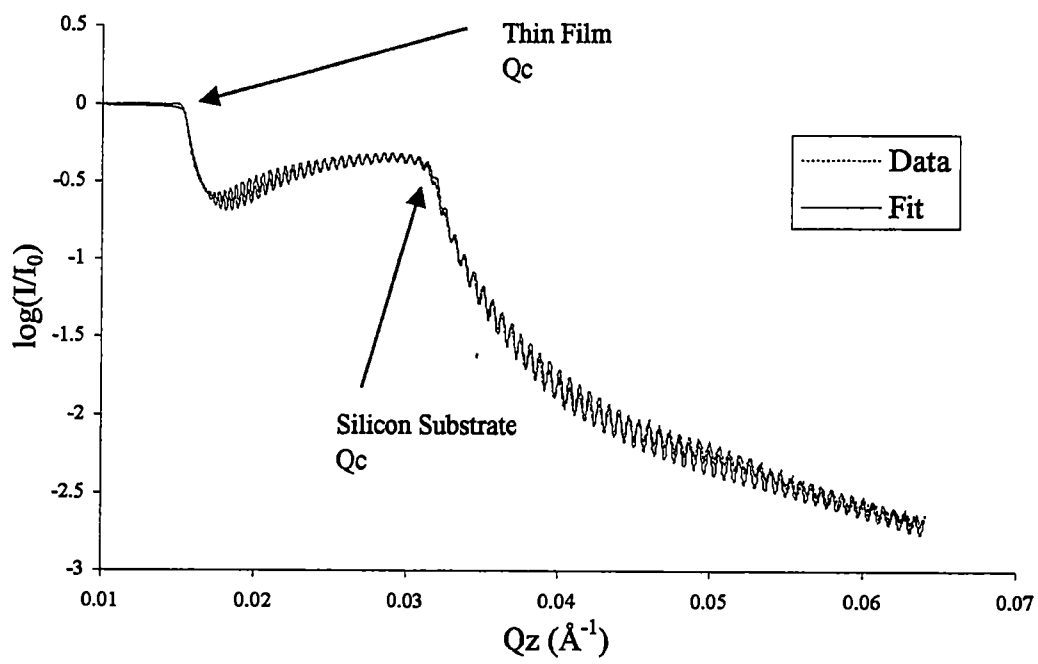


Figure 2.2. X-ray reflectivity result for the sample

calculated from $\theta_c = (\rho_e \lambda^2 / \pi)^{1/2}$. Using $Q_z = 0.0155 \text{ \AA}^{-1}$, an electron density of $1.693 \times 10^{23} \text{ e}^-/\text{cm}^3$ for the porous silica thin film is calculated. $1.693 \times 10^{23} \text{ e}^-/\text{cm}^3$ is the mean electron density for the overall film thickness, which includes the pores, and pore wall material. Given the chemical composition of the film from the ion beam scattering measurements, the mean electron density can easily be converted to a mass density. For this particular Allied Signal Nanoglass™ sample, the mass density is calculated to be $(0.55 \pm 0.01) \text{ g/cm}^3$.

$(0.55 \pm 0.01) \text{ g/cm}^3$ is the mass density for the overall film. As of right now, we do not have independent information for the pore wall material density, ρ_w , or for the porosity, P . P can be estimated if we assume that $\rho_w = 2.25 \text{ g/cm}^3$, which is the mass density of a typical thermal oxide, then the corresponding porosity is 75.6% by volume. Another hypothesis might be that the pore wall material is hydrogen silsesquioxane (HSQ), a spin-on silica based glass material with a mass density of 2.00 g/cm^3 , then the porosity would be 72.6% by volume. However, our film is not purely silica. It contains a significant fraction of hydrocarbons as revealed by the chemical composition analysis, so ρ_w for our film should differ from that of the thermal oxide or the HSQ. In addition, the density for a thermal oxide or HSQ can vary dramatically since both are dependent on processing conditions [61].

One might think that measurements of 75.6% or 72.6% might be sufficiently accurate as a measure of the porosity. However, industry needs an even more accurate measurement of the porosity because the dielectric constant can change by as much as a tenth between 75.6% and 72.6%. Using a complementary experimental technique, we can test the validity of our wall density assumptions. According to our two-phase model,

if P is the volume fraction occupied by the pores, then $(1 - P)$ is the volume fraction occupied by the pore wall material. The overall thin film mass density, which again includes the pores and pore wall material, is simply the product of the pore wall material density and the volume fraction occupied by the pore wall material, $\rho_w(1 - P)$. We have thus far determined only the overall thin film mass density from X-ray reflectivity and composition data. A second independent technique is needed to obtain another measurable quantity that is related to both ρ_w and P . Right now, we have two unknowns with only one equation. We need a second equation to solve for the two unknowns. With two independent measurements that contain both ρ_w and P in different forms, we can solve the equations simultaneously to get the values of our two unknowns ρ_w and P . SANS is the experimental technique we chose to fulfill this need. SANS results can also provide information related to the size of the pores.

Pore Wall Density and Pore Structure

Debye et al. [62] developed a density correlation function for a random two-phase structure which is $\gamma(r) = \exp(-r/\xi)$ where \exp is the exponential function, r is an arbitrary distance, and ξ is the correlation length of the two-phase system. The correlation length is a measure of the distance over which the concentration fluctuations remain correlated, and is defined as

$$\xi = 4[V/S][\langle \eta^2 \rangle / (\Delta\rho_n)^2], \quad (2.1)$$

where V is the scattering volume, S is the total surface area of the boundaries between the two phases, $\langle \eta^2 \rangle$ is the mean square of the fluctuations and $\Delta\rho_n$ is the difference in neutron scattering length density between the two phases. The ratio V/S has dimension

of length (volume/area) and can be regarded as the length scale that characterizes the structure. Details on the mean square of the fluctuations are provided in Section 1 of the Appendix (A.1). Substituting $\langle \eta^2 \rangle = (\Delta\rho)^2 \phi_1 \phi_2$ from Equation A.1.17 into Equation 2.1, the correlation length is

$$\xi = 4[V/S][\phi_1 \phi_2], \quad (2.2)$$

where ϕ_1 and ϕ_2 are the volume fractions of phases 1 and 2. The average dimension of phase 1 and phase 2 are related to V/S by

$$\langle L_1 \rangle = 4(V/S)\phi_1 \text{ and } \langle L_2 \rangle = 4(V/S)\phi_2. \quad (2.3)$$

For our two-phase system, $\phi_1 = P$ and $\phi_2 = (1 - P)$. If ξ is the correlation length for the two-phase system, then $\xi/(1-P)$ is the average dimension of the pores and ξ/P is the average dimension of the pore wall material. Figure 2.3 shows a schematic of the correlation length, average dimension of the pores and pore wall material. One can think of a density correlation like this: If we have two distinct phases r_1 and r_2 with densities ρ_1 and ρ_2 , and if we start at a point in r_1 with a density of ρ_1 , what is the probability that we will encounter another point r distance away with the same density ρ_1 ? According to Debye's density correlation function, this probability not only becomes smaller the farther the distance r from a point, but this probability also decays exponentially. Since these silica thin films are composed of pores with a high volume content, the Debye density correlation function is a suitable model to describe the structure that we are dealing with in our silica thin films. The scattered intensity based on this model takes the form of

$$I(q) = 8\pi P(1-P)\Delta\rho_n^2 \xi^3 / (1+q^2 \xi^2)^2, \quad (2.4)$$

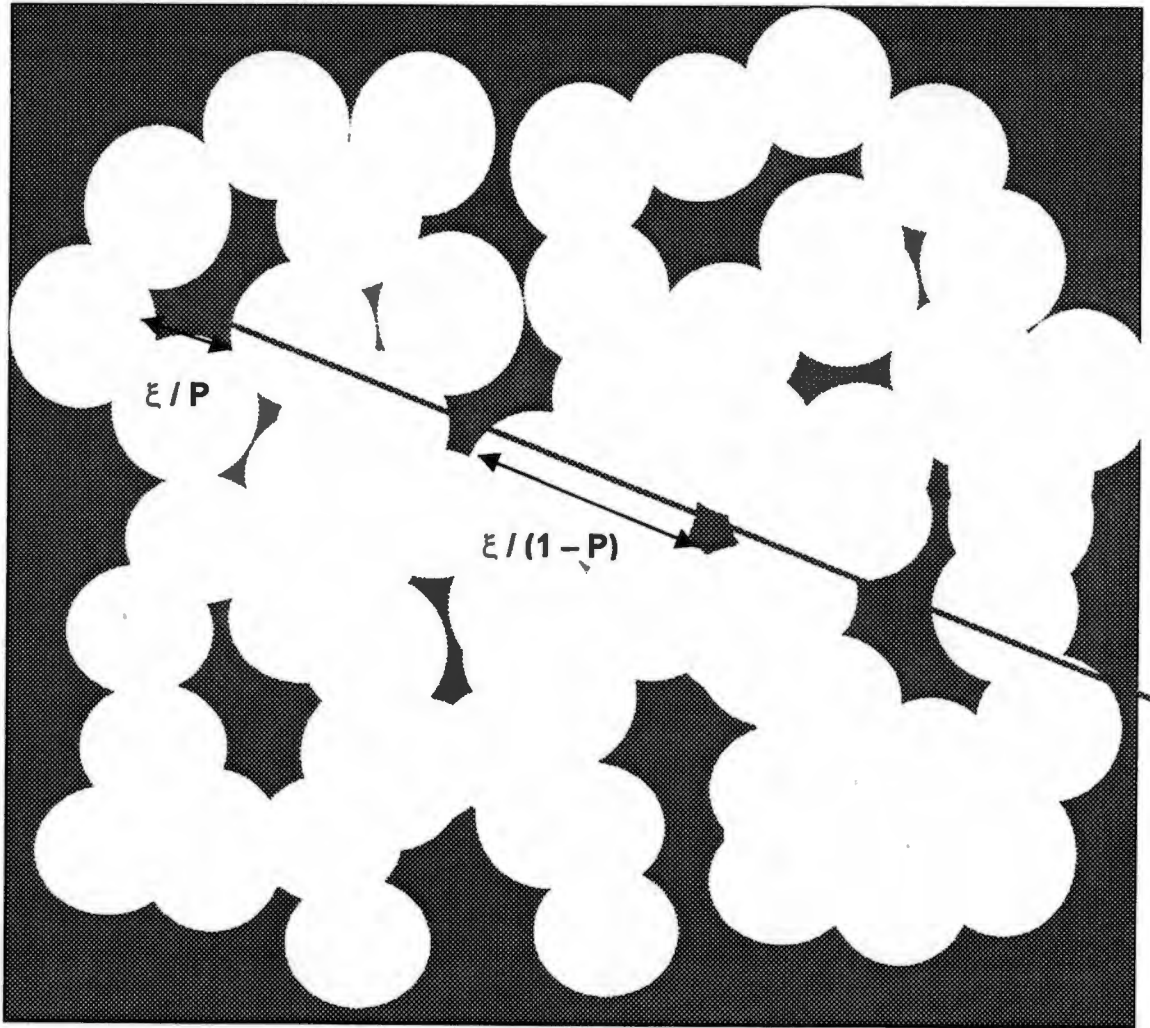


Figure 2.3. Schematic depicting the correlation length, average dimension of pores and pore wall material

where $\Delta\rho_n$ is the neutron scattering length contrast between two phases. The derivation of Equation 2.4 from first principles of scattering is included in Section A.1 of this thesis. For our case, the neutron scattering length contrast, $\Delta\rho_n$, is simply the neutron scattering length of the pore wall material because the neutron scattering length of the pores is zero. More explicitly, $\Delta\rho_n$ equals ρ_{wn} , the neutron scattering length of the pore wall material. ρ_{wn} is equal to $(\sum n_i b_i / \sum n_i m_i) \rho_w$, where n_i is the atomic fraction of element i , b_i is the neutron scattering length of element i , m_i is the atomic weight of that element and ρ_w is the mass density of the pore wall material. Given this relationship and the chemical composition from ion scattering measurements, only ρ_w , a parameter of interest, is unknown. In other words, the neutron scattering length contrast, $\Delta\rho_n$, is the neutron scattering length of the pore wall material, ρ_{wn} , which in turn can easily be converted to the mass density of the pore wall material, ρ_w , if the chemical composition of the pore wall material is known. So the question becomes, how do we obtain ρ_w from the SANS intensity? In order to extract information from the SANS experimental data, Equation 2.4 is rearranged to get:

$$1/I(q)^{1/2} = 1/(c\xi^3)^{1/2} + \xi^2 q^2 / (c\xi^3)^{1/2}, \quad (2.5)$$

where c is defined as $8\pi P(1-P)\Delta\rho_n^2$. Equation 2.5 is in the form of a straight line ($y = mx + b$) where $y = 1/I(q)^{1/2}$, $x = q^2$, $m = \xi^2 / (c\xi^3)^{1/2}$ and $b = 1/(c\xi^3)^{1/2}$. The two quantities, c and ξ , from Equation 2.5 can be determined from the slope ($\xi^2 / (c\xi^3)^{1/2}$) and the zero q intercept ($1/(c\xi^3)^{1/2}$) from a straight line fit of the SANS data plotted as $I(q)^{-1/2}$ vs. q^2 . The correlation length, ξ , is equal to $(\text{slope}/\text{intercept})^{1/2}$. Once ξ is known, the quantity c is calculated from the intercept and ξ . The quantity c is related to both P and ρ_w by

$8\pi P(1 - P)\rho_w^2$, since $\Delta\rho_n$ can be converted to ρ_w from the composition analysis. In the previous section, the overall thin film mass density is given by $\rho_w(1 - P)$, and has already been measured using X-ray reflectivity. We have our two independent equations from two different measurements.

Figure 2.4 shows a plot of the SANS data as $I(q)^{-1/2}$ vs. q^2 and the straight line fit. As can be seen from Figure 2.4, Equation 2.5 seems valid except in the low q region. We believe that the observed scattering in the low q region may be associated with a nonuniform distribution of the pores, or with larger length scale heterogeneities, e.g., clustering of the pores. Therefore, one's selection of the q region in which to fit a straight line becomes important. The q region must be selected so as not to fit a straight line where the signal is dominated by larger length scale heterogeneities. Likewise, if one fits a straight line in the higher q region, the signal is dominated by local structure and the results will be erroneous. The slope and $q = 0$ intercept of the straight-line fit in Figure 2.4 are calculated to be $(163.2 \pm 0.9) \text{ cm}^{1/2} \text{ \AA}^2$ and $(0.175 \pm 0.002) \text{ cm}^{1/2}$. Given the slope and intercept of the straight line fit from the SANS data, the correlation length, ξ , is 30.5 \AA ($\xi = [163.2/0.175]^{1/2}$) and c is $1.15 \times 10^{21} \text{ cm}^{-4}$ ($c = \{[1/\text{intercept}]^{1/2}/\xi^3\}$). The fact that we obtain a correlation length of 30.5 \AA verifies that we are fitting in the correct q region. Correlation lengths of 3.05 \AA or 305 \AA are not physically possible for the size of the pores. The quantity c is also equal to $8\pi P(1 - P)\rho_w^2$. Dividing c by $8\pi\rho_w^2$, one obtains $P(1 - P)$, where ρ_w is the scattering length density of the material with composition as measured from the ion beam scattering. The overall thin film mass density from the X-ray reflectivity data is 0.55 g/cm^3 , which is also equal to $\rho_w(1 - P)$.

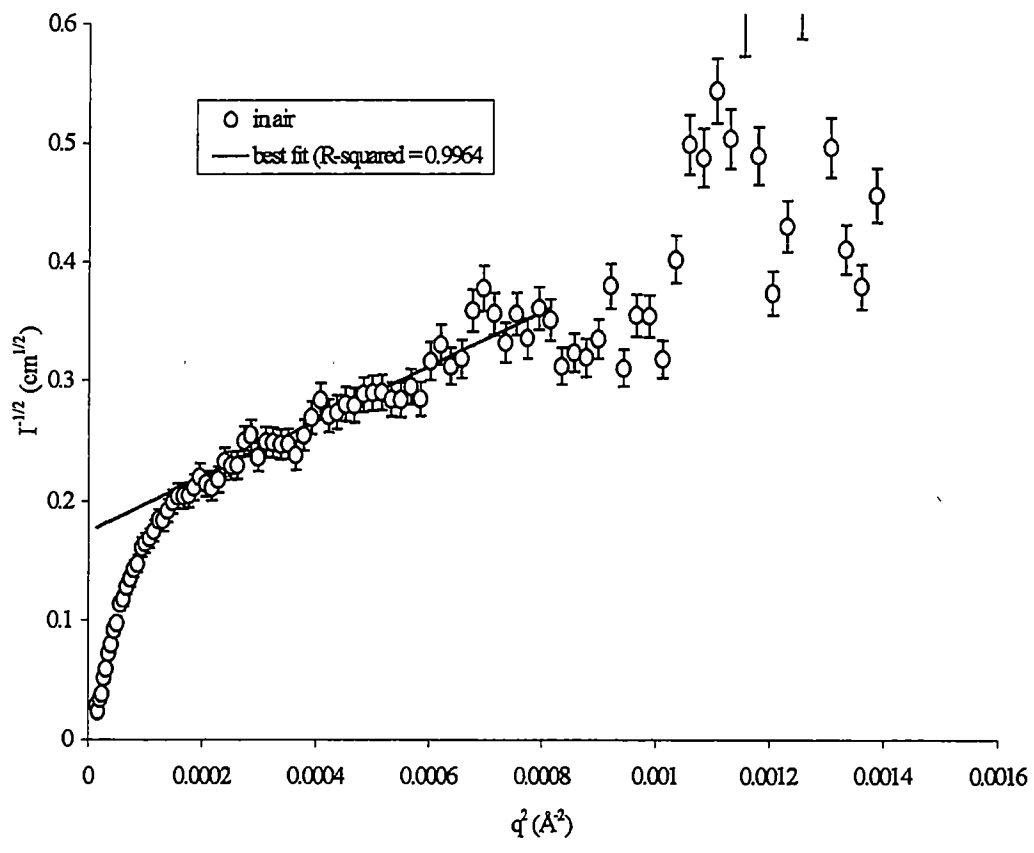


Figure 2.4. Debye plot for the sample in air

The density of the pore wall material, ρ_w , is $(1.16 \pm 0.05) \text{ g/cm}^3$. The volume fraction occupied by the pore wall material is equal to $\rho_w(1 - P)/\rho_w$. Once the volume fraction of the pore wall material is known, then the porosity is just $1 - (1 - P)$. The porosity, P , for our sample is determined to be $(53 \pm 1) \%$ with an average dimension of the pores as $(65 \pm 1) \text{ \AA} (\xi/P)$.

Pore Interconnectivity

If a large fraction of pores have passage to the exterior surface, then the probability of contamination during the CMP process is greater. Therefore, it is advantageous to know the pore interconnectivity. After determining the porosity and pore wall density from the SANS data for the sample in air, we would like to determine the interconnectivity of the pores. What fraction of the pores have passage to the exterior surface of the film? SANS measurements were conducted on the same thin film sample except now the sample was immersed in *d*-toluene, as *d*-toluene completely wets the film. If all the pores are filled with the *d*-toluene, then this SANS intensity is easily related to the SANS intensity for the sample in air. The SANS intensity at $q = 0$, ($I(q = 0)$), is equal to $1/(c\xi^3)^2$. The quantity c is also equal to $8\pi P(1 - P)\Delta\rho_n^2$, so the intensity at $q = 0$ gives the contrast factor which is related to the density of the material. The SANS contrast factor in Equation 2.4, $\Delta\rho_n^2$, for the sample in air, is the difference in neutron scattering length of the pore wall material and air. If all the pores were filled with *d*-toluene, then the contrast factor is the difference in neutron scattering length of the *d*-toluene and pore wall material $(\rho_{\text{dtol}} - \rho_{\text{pwm}})^2$. Since *d*-toluene has a higher neutron scattering cross-section than air, the contrast should be enhanced. In fact, given the scattering length density of *d*-

toluene, the contrast factor should increase by a factor of 18.3 over air. However, Figure 2.5 shows that this is not the case, and the increase in intensity is less than a factor of 18.3. Furthermore, the average pore size calculated for the *d*-toluene immersed sample differs from that of the sample in air. The reason for this may be that not all the pores are being filled by the *d*-toluene, and that only a select population of pores is being filled. This select population will be the pores connected to the surface of the film. If only a fraction of the pores is being filled, then what is that fraction? In order to estimate the fraction of filled pores, we decided to use a two-layer model. We assume that the film immersed in *d*-toluene is made up of two layers. One layer is wetted with the *d*-toluene and all the pores are filled. The other layer is dry and none of the pores are filled. An alternative model for a partially filled system might be a random model in which all the filled and unfilled pores are intermixed and randomly distributed. We chose not to use the random model because in the random model, an empty pore adjacent to a filled pore has a greater probability of also being filled. Now that we have settled on what we believe to be an appropriate model for our system, how can we equate the model to the measured scattering intensity? Our scattering intensity will come from a combination of the dry layer plus the wet layer, or in other words, the unfilled pores plus the filled pores. If we let Φ be equal to the volume fraction of the thin film wetted layer, then $(1 - \Phi)$ will be the volume fraction of the dry layer. The scattering intensity at $q = 0$ for the sample immersed in toluene is thus,

$$I_{\text{dtol}}(q = 0) = (1 - \Phi)\rho_{\text{pwm}}^2 P(1 - P) + \Phi(\rho_{\text{dtol}} - \rho_{\text{pwm}})^2 P(1 - P), \quad (2.6)$$

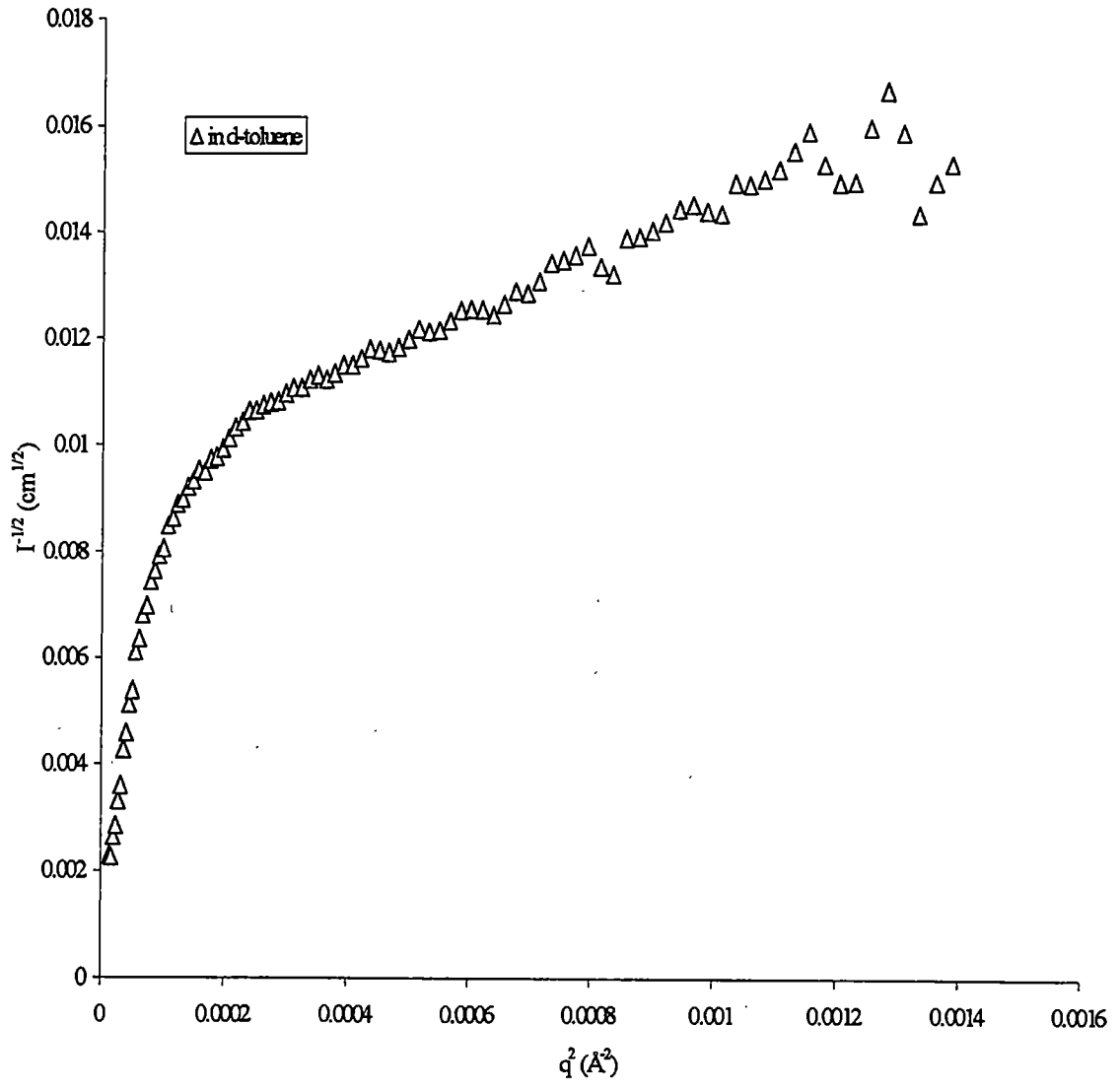


Figure 2.5. Debye plot for the sample in d-toluene

where ρ_{dtol} is the neutron scattering length of toluene. P is the volume fraction of the unfilled pores, $(1 - P)$ is the volume fraction of the pore wall material and ρ_{pwm} is the neutron scattering length for the pore wall material. The first term in Equation 2.6 is for the dry layer. Note that the quantity $\rho_{pwm}^2 P(1 - P)$ is the same as for the sample in air as in Equation 2.4. As was mentioned earlier, ρ_{pwm}^2 is the same as $\Delta\rho_n^2$ because the scattering length of air is zero. Following this analysis, the sample consists of two layers; the total scattering from the unfilled pores is the product of the fraction of unfilled pores, $(1 - \Phi)$, and $\rho_{pwm}^2 P(1 - P)$, while the contrast factor for the wet layer is the difference of the d -toluene scattering length, ρ_{dtol} , and the pore wall material scattering length, ρ_{pwm} . This contrast factor, $(\rho_{dtol} - \rho_{pwm})^2$, is multiplied by $\Phi P(1 - P)$ to account for the pore fraction that is filled by the d -toluene. If all the pores were filled by d -toluene, then the predicted intercept, $I_{dtol}(0) = [I_{air}(0)][(\rho_{dtol} - \rho_{pwm})^2 / \rho_{pwm}^2]$, where $I_{air}(0)$ is the intensity at $q = 0$ for the sample in air. The fraction of pores filled by d -toluene is then equal to $[measured\ I_{dtol}(0) - I_{air}(0)] / [predicted\ I_{dtol}(0) - I_{air}(0)]$. For this sample, the value of Φ , the volume fraction of pores filled by d -toluene, was calculated to be $(22.1 \pm 0.05)\%$. Thus, 22.1 % of the pores are interconnected with access to the exterior surface of the film.

Moisture Uptake

In order to estimate the moisture uptake of the thin film, a new sample was placed in D_2O for 24 hours at room temperature. The same two-layer model as in the d -toluene case was used to analyze the SANS data for the sample in D_2O . Again, the intensity at $q = 0$ and Equation 2.6 is utilized to determine the value Φ with the substitution of the

scattering length of D_2O , ρ_{D_2O} , for ρ_{dtol} . In this manner, Φ is the volume fraction of pores that are filled with D_2O . Compared to the *d*-toluene sample, the sample immersed in D_2O did not result in significant increases in the SANS intensities from the sample in air (see Figure 2.6). This result was not surprising since the films are macroscopically hydrophobic. A drop of distilled water on the surface of the film displays a rather large contact angle. Quantitative analysis of the SANS data reveals that (3.10 ± 0.05) % of the pore volume inside the film was filled with D_2O .

Coefficient of Thermal Expansion

Specular X-ray reflectivity data is an excellent technique for measuring the out of plane coefficient of thermal expansion (CTE). The thickness of a film is readily determined from the spacing of the interference fringes in a reflectivity spectrum. Details of this fact will be elucidated in section 2 of the appendix. The porous film was placed in a vacuum in a specially designed chamber and the film thickness was measured at different temperatures. The reflectivity measurements were conducted under vacuum in order to minimize thermal degradation or oxidation of the film. Before each measurement, the sample was held at the measurement temperature for at least 1 hour in order to ensure thermal equilibrium. The thin film CTE is determined by the dependence of the film thickness with temperature. In the X-ray reflectivity data shown of Figure 2.2, many oscillations occur between the two critical angles or Q_z ($0.0155 \leq Q_z(\text{\AA}^{-1}) \leq 0.0320$). These oscillations are a manifestation of optical coupling. At certain incident angles, the thin porous film acts as a X-ray wave-guide. The incident beam travels within the film with little intensity escaping from the film. This phenomenon causes the minima in the reflected intensity in the wave-guide region. At angles greater than the critical

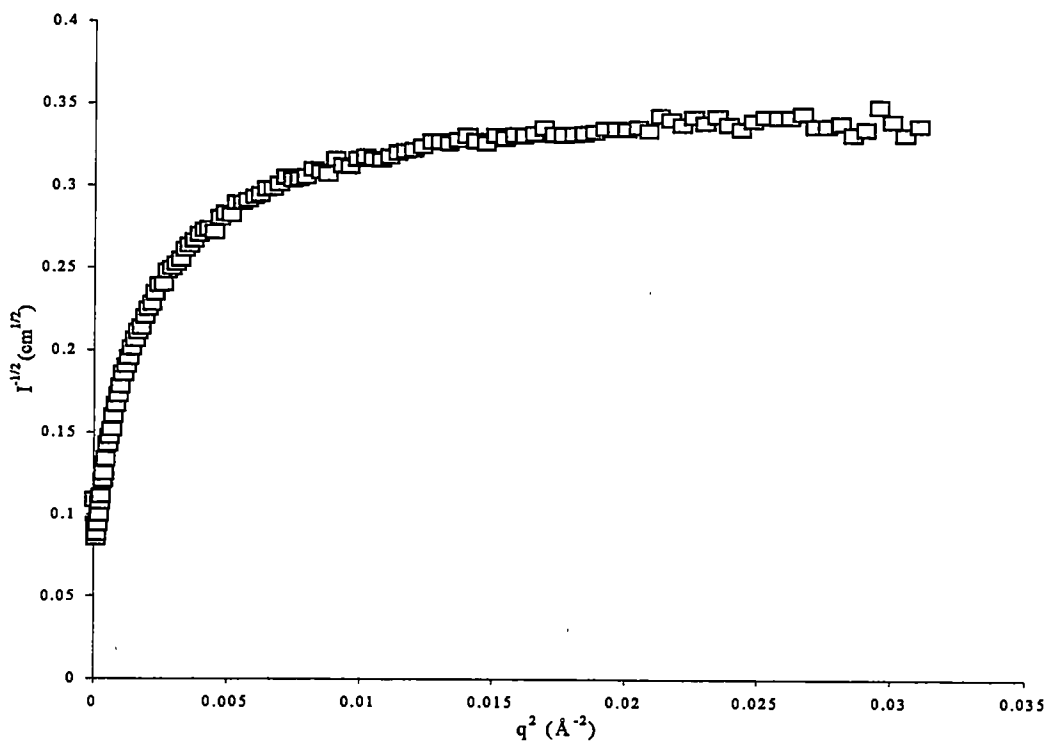


Figure 2.6. Debye plot for the sample immersed in D2O

angle or critical Q_z (0.0320 \AA^{-1}) of the silicon substrate, the oscillations are due to the interference of radiation reflected from the air / film and film / silicon substrate interfaces. In the low Q_z region or region close to the critical Q_z of the silicon substrate, the relationship between film thickness and spacing of the fringes is not strictly true due to multiple scattering. Therefore, the film thickness is best determined from the periodicity of the interference fringes in the high Q_z region. For our work, we defined the start of the high Q_z region to be where the reflectivity falls below 10^{-2} . Sampling of the periodicity of the fringes was taken from this point to the end of the measured data. In this region, multiple scattering constitutes less than 1% of the total reflected intensity. In order to determine the film thickness from the periodicity of the fringes, a Fourier transform (FT) is performed on the high Q_z data. Figure 2.7 shows this Fourier transform for the film at 25 °C and the thickness is calculated by multiplying the peak position of the FT by 2π (See Equation A.2.18). The measured film thickness at various temperatures ranging from 25 to 175 °C was determined and is shown in Figure 2.8. The CTE as calculated from the slope of the best-fit line to the data is $(60 \pm 20) \times 10^{-6}/^\circ\text{C}$. The uncertainty is due largely to the 10nm uncertainty in the measurement of film thickness. The measurement of thicker films or of films with a higher CTE decreases the uncertainty of the CTE value itself. By comparison, the CTE of single crystal silicon (our silicon substrate) is $3 \times 10^{-6}/^\circ\text{C}$.

Conclusion

We have successfully developed a methodology to characterize the structural properties of porous thin silica films on the order of $1\mu\text{m}$ thick and supported on silicon

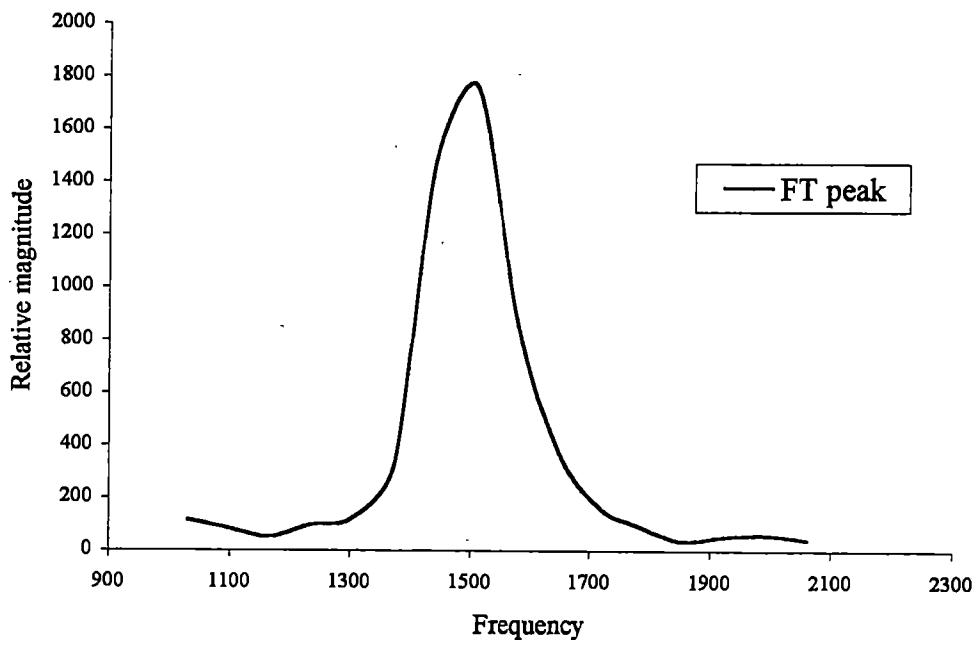


Figure 2.7. Fourier transform of the reflectivity fringes

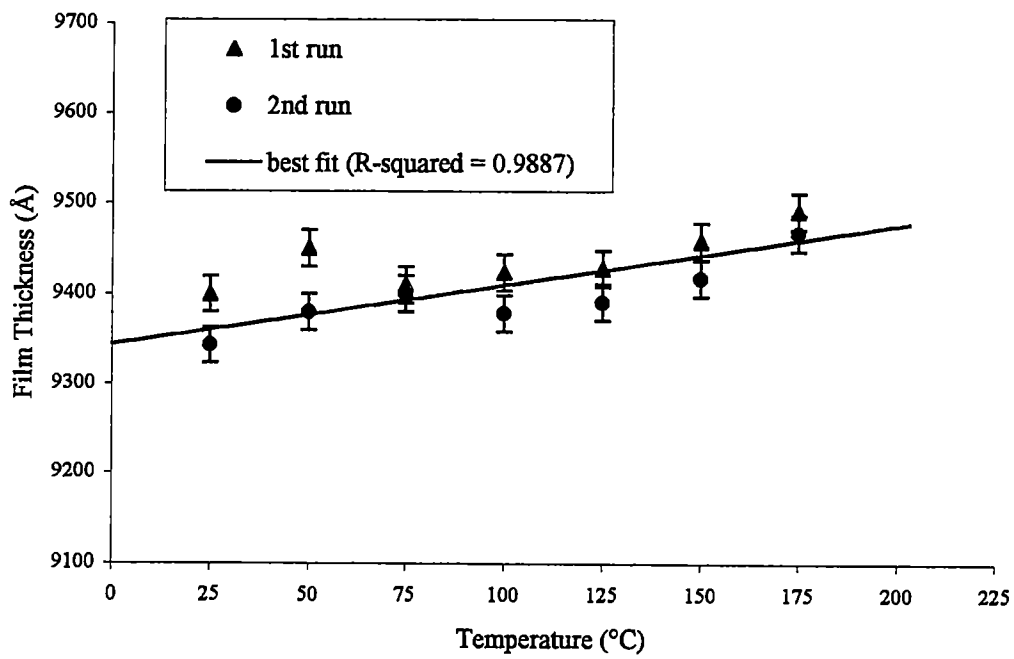


Figure 2.8. Film thickness vs. Temperature

substrates. Our method was demonstrated using Allied Signal's Nanoglass™ K2.2-A10B and has been used to characterize 20 porous silica thin films provided by SEMTECH. A combination of specular X-ray reflectivity and ion beam scattering provided an average mass density of $(0.55 \pm 0.01) \text{ g/cm}^3$ for the overall film. SANS, in combination with specular X-ray reflectivity and ion beam scattering provided a film porosity of $(53 \pm 1) \%$, a pore wall density of $(1.16 \pm 0.05) \text{ g/cm}^3$, an average pore size of $(65 \pm 1) \text{ \AA}$, a pore connectivity of $(22.1 \pm 0.05) \%$ and $(3.10 \pm 0.05) \%$ of the pores filled by water. Precise measurement of the film thickness and an out of plane CTE of $(60 \pm 20) \times 10^{-6}/^\circ\text{C}$ was determined by specular X-ray reflectivity.

Chapter 3

Neutron Reflectivity at a Small Molecule Liquid Crystal / Polymer Interface

This chapter describes how we used neutron reflectivity to determine the structure of a small molecule liquid crystal / polymer interface. More specifically, we examined the interfacial transition zone width of a small molecule liquid crystal/polymer interface as a function of increasing temperature. Section 3.1 is an introduction and outline for our motivation followed by the experimental set up in section 3.2. A discussion of our results is given in section 3.3.

3.1

Introduction

Important areas of liquid crystal display (LCD) technology include the use of polymer-stabilized liquid crystals and polymer dispersed liquid crystals (PDLC) [63]. PDLC systems typically consist of a five to ten weight percent liquid crystal dispersed homogeneously in a cross-linked polymer matrix. The confined liquid crystal droplets reside in cavities formed during the polymerization process. In the absence of an electric field, the directors of the liquid crystal are randomly oriented and the material is opaque due to the difference between the refractive indices of the matrix and droplets. When an electric field is applied, the directors align themselves to a preferred orientation and the material becomes transparent if the refractive index of the matrix and effective refractive index of the liquid crystal are very similar. Since PDLC materials exhibit a large surface to volume ratio, surface, rather than bulk, properties dominate the optical characteristics of the device. The specific nature of the liquid crystal/polymer interface controls the surface induced orientation of the liquid crystal, a parameter that affects the ultimate

optical properties of the display device. Even though the nature of the liquid crystal/polymer interface strongly influences the optical properties of the resulting structure, there exists very little experimental characterization of these liquid crystal/polymer interfaces.

Numerous experiments have looked at the thermodynamic and structural behavior of 8CB in confined geometries in order to study liquid crystal interface properties [64]. A few examples of the many experiments include Hikmet and Howard who used IR dichroism to examine 8CB in anisotropic gels and plasticized networks [65]. They found that a fraction of the 8CB molecules remained oriented above the nematic to isotropic transition temperature. A bound fraction of 8CB was largely influenced by the network and did not show a first order nematic to isotropic transition. Iannacchione and Finotello used an AC calorimetry technique [66] to measure specific heats of the mesophases of 8CB in Anopore membranes. They concluded that the nematic to isotropic transition strongly depends on the liquid crystal director orientation within an Anopore membrane. Bellini *et al.* and Clark *et al.* have studied 8CB in silica aerogels using light scattering, precision calorimetry and x-ray scattering to show the nematic and nematic to smectic-A translational ordering [67,68]. Their results show that nematic ordering of 8CB in the pores of a silica aerogel does not occur as a first order phase transition like that in the bulk. Experiments of 8CB confined in porous glasses has been looked at by Iannacchione *et al.* via AC calorimetry, DSC and small angle neutron scattering as well as Sinha and Aliev using dielectric spectroscopy [69,70]. Iannacchione *et al.* showed that for 8CB in a Vycor glass, the nematic to isotropic transition is a continuous transition and not first order. Sinha and Aliev showed that at the nematic to isotropic transition,

some degree of orientational order of the 8CB still persists. This result of 8CB in a porous glass is in contrast to that of 8CB in the bulk. The bulk 8CB isotropic phase exists in complete disorder. Finally, Dadmun and Muthukumar [71,72] have examined the nematic to isotropic transition of liquid crystals in a controlled pore glass and near an adsorbing surface. Both of these experiments show the importance of a smooth wall on the orientation of the liquid crystal, as well as the importance of confinement on the order-disorder transition.

In most studies of the interface near liquid crystals, the liquid crystal interface is treated as being very sharp. This treatment is implied in theories ranging from a thermodynamic approach to statistical mechanical and phenomenological approaches [73]. Assuming that the interface between a liquid crystal and materials such as silica aerogels and porous glasses in theories and simulations is sharp is valid. However, this may not be the case for systems where the structure is formed by the phase separation of a liquid crystal and polymer mixture.

Thus, we report in this manuscript information on the structure of the interface between a polymer and small molecule liquid crystal. More specifically, neutron reflectivity will be used to determine the structure of the interface between a small molecule liquid crystal, 8CB and poly(methyl methacrylate). It is hoped that the results presented here will be useful in future experimental and theoretical studies of devices that are formed from small molecule liquid crystal/polymer mixtures. The choice of system was governed by the desire to mimic commercially relevant PDLC or PSLC materials. The cyanobiphenyls, a class of small molecule liquid crystals, are commonly used in PDLC materials. These liquid crystals usually offer nematic to isotropic transitions

around room temperature, which becomes important when minimizing the operating voltage. At temperatures farther away from the nematic to isotropic transition, surface anchoring and elastic deformation forces begin to dominate and it becomes increasingly difficult to align the directors of the liquid crystal with an applied electric field. For our system we chose the small molecule liquid crystal 4'-n-octyl-4-cyanobiphenyl (8CB). The 8CB transitions include a crystalline to smectic-A transition at 21.5 °C, a smectic-A to nematic transition at 33.5 °C and a nematic to isotropic transition at 40.5°C [74]. The acrylates, a class of polymers, are used extensively in PDLC applications as well. The acrylates typically have refractive indexes comparable to the small molecule liquid crystals, while ease of cross-linking is another advantage when using the acrylates. The structure of cross-linked networks is usually unaffected by temperature or an applied electric field. In our study deuterated poly(methyl methacrylate) (*d*-PMMA) has been used as the polymer matrix. The deuteration of the PMMA provides contrast for the neutron reflectivity and *d*-PMMA is also readily available. One area where our system differs from those used in PDLC or PSLC optical devices is that our system is not cross-linked. Unfortunately, there are many complications and difficulties associated with spin coating a cross-linked thin film polymer, such as not knowing the degree of cross-linking and forming a uniform sample that is suitable for reflectivity. Thus, we have been unable to complete reflectivity studies on cross-linked *d*-PMMA.

3.2

Experimental

Sample Preparation

A three-layered sample was prepared on a polished silicon wafer (102 mm in diameter, 6 mm thick). As shown in Figure 3.1, the sample consisted of a layer of 8CB on top of the silicon wafer followed by a layer of *d*-PMMA and topped off with a layer of aluminum metal. The silicon wafer ($\{111\}$ n-type) was first placed in a buffered etch solution to remove the native oxide layer from the polished surface. The wafer was then placed in a UV/ozone cleaner to remove any organic impurities and to regrow a native oxide surface. The 8CB was purchased from Aldrich [75] and used without further purification. A smectic-A to nematic transition and nematic to isotropic transition at temperatures of $33.1 \pm 0.2^\circ\text{C}$ and $40.1 \pm 0.2^\circ\text{C}$ respectively, were determined using a Mettler Toledo DSC821^o differential scanning calorimeter (DSC). The 8CB was spin cast onto the silicon wafer from a toluene solution with a 8CB mass fraction of 2%. The sample was covered and placed in a freezer. The *d*-PMMA (M_w 169,604, M_w/M_n 1.09) was purchased from Polymer Source Inc. and used as received. DSC measured a glass transition temperature of $(90.66 \pm 0.5)^\circ\text{C}$ for this polymer at a heating rate of $10^\circ\text{C}/\text{min}$. A glass micro slide (75 x 50 mm) was wiped clean with acetone and then placed in the UV/ozone cleaner. The *d*-PMMA was spin cast onto the glass micro slide from an *o*-xylene solution with a *d*-PMMA mass fraction of 3.5%. The thin film of *d*-PMMA was then floated onto the 8CB layer from the glass micro slide in $18\text{ M } \Omega\cdot\text{cm}$ chilled water. This two-layer sample was then placed in a desiccator under vacuum and at room temperature overnight. A 1000 \AA

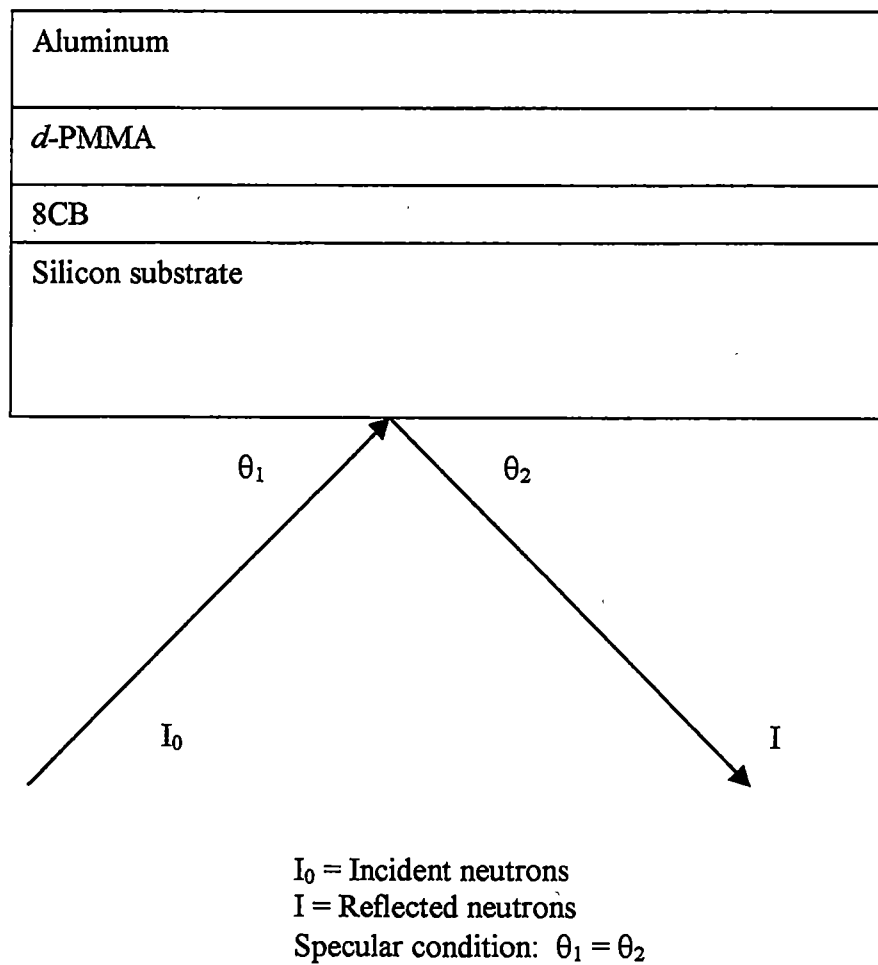


Figure 3.1. Depiction of the various thin films and their arrangement on the silicon substrate (not drawn to scale)

thick film of aluminum metal was evaporated on top of the *d*-PMMA to ensure that none of the 8CB escaped from the system during thermal treatments of the experiment.

Neutron Reflectivity

Specular neutron reflectivity measurements were performed on the sample at the National Center for Neutron Research (NCNR) NG-7 reflectometer at the National Institute of Standards and Technology in Gaithersburg, MD. The wavelength (λ) of the neutrons was 4.768 Å with a wavelength spread ($\Delta\lambda/\lambda$) of 0.2. The sample was placed on a heating stage in a vacuum tight chamber. The neutron beam was passed up through the silicon wafer and out the aluminum/vacuum interface (see Figure 3.1). The ratio of reflected intensity to incident beam intensity (reflectivity) was measured from the silicon wafer/8CB interface parallel at grazing incidence angles between 0.11° and 2.6°. The reflectivity is plotted as a function of the neutron momentum transfer normal to the surface of the sample (Q_z), where $Q_z = (4\pi/\lambda) \sin(\theta)$ and θ is the incident angle. The neutron scattering length density profile normal to the sample surface can then be determined from the measured reflectivity. Furthermore, it is the elastic coherent scattering per unit volume (Q_c^2) which determines this density profile normal to the surface, where $Q_c^2 = 16\pi n b$ and n is the number density of scattering nuclei ($N_A \rho/M$), b is the neutron scattering length, N_A is the Avogadro constant, ρ is mass density of the species and M is the molar mass of the species. The scattering length density profile is calculated from model fits of the measured reflectivity data. The model fits are determined using a recursive multilayer method [76]. It is necessary to fit the data because like conventional diffraction, one cannot know both the amplitude and phase of

the reflected beam. Further details concerning the reflectivity technique are available in the literature [77].

3.3

Results and Discussion

The purpose of this project is to determine the width of the interface between the small molecule liquid crystal and the polymer and its response to a change in temperature. Therefore, the reflectivity of the trilayer sample was measured at a series of temperatures. All temperatures reported below are accurate to within ± 1.0 °C. The sample was held at each temperature for 45 min before measuring the reflectivity in order to reach thermal equilibrium. The duration of each measurement was 2 hr and 15 min. The sample was also kept at a constant pressure of 5.5×10^{-5} torr during the experiment.

The reflectivity was first measured at 25 °C, and then measured at 50 °C and 75 °C. This was followed a second measurement at 75 °C to ensure that the sample was not changing in the total 3 hr period that it took to measure the reflectivity. Figure 3.2 shows that these two curves obtained at 75 °C are indeed identical and demonstrate that the layered structure may change with temperature, but do not change in the course of the experiment. A fifth measurement of the reflectivity was also made at 110 °C. Figure 3.3 and Figure 3.4 show the measured reflectivity curves at 25, 50, 75 and 110 °C.

Inspection of the reflectivity curves can provide quite a bit of information regarding the multi-layer structure. The measured reflectivity curve is a convolution of the reflected intensities from the individual interfaces of the 8CB, *d*-PMMA and Al layers. The spacing of the interference fringes present in the curve is determined by the

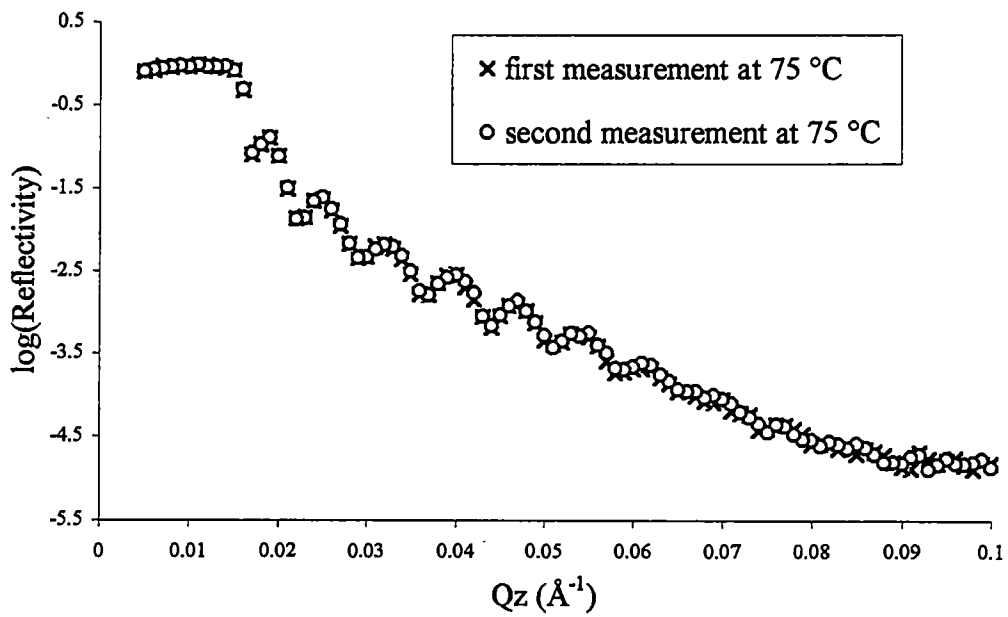


Figure 3.2. Neutron reflectivity data measured consecutively at 75 °C

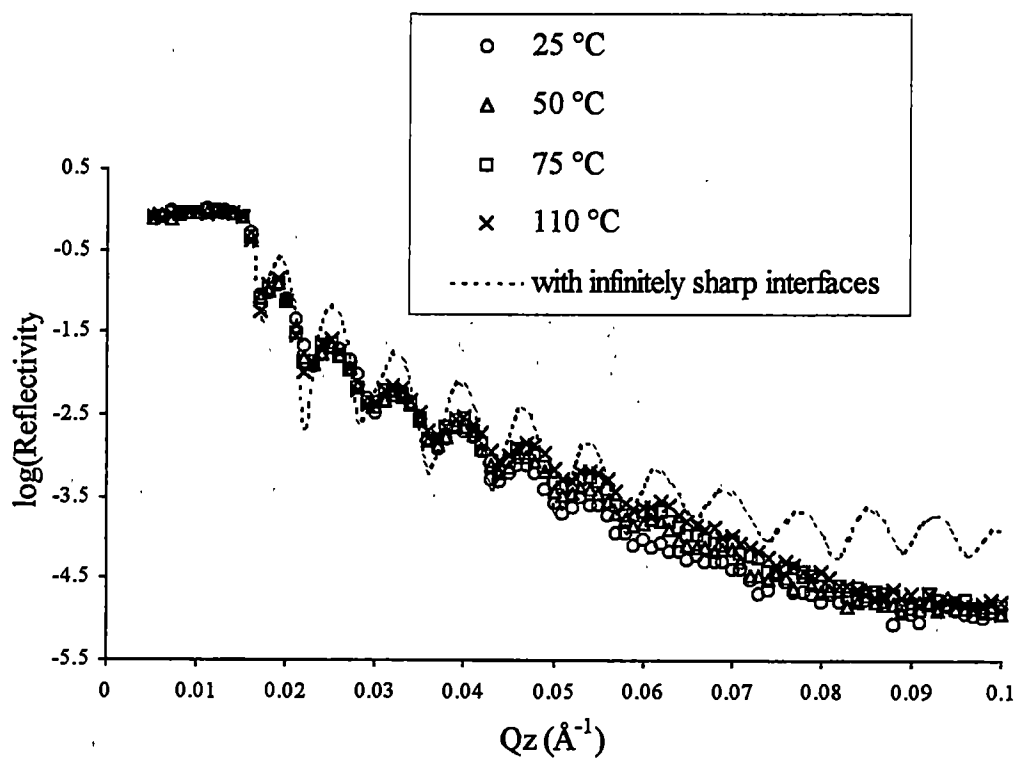


Figure 3.3. Neutron reflectivity data measured at (25,50,75 and 110) °C

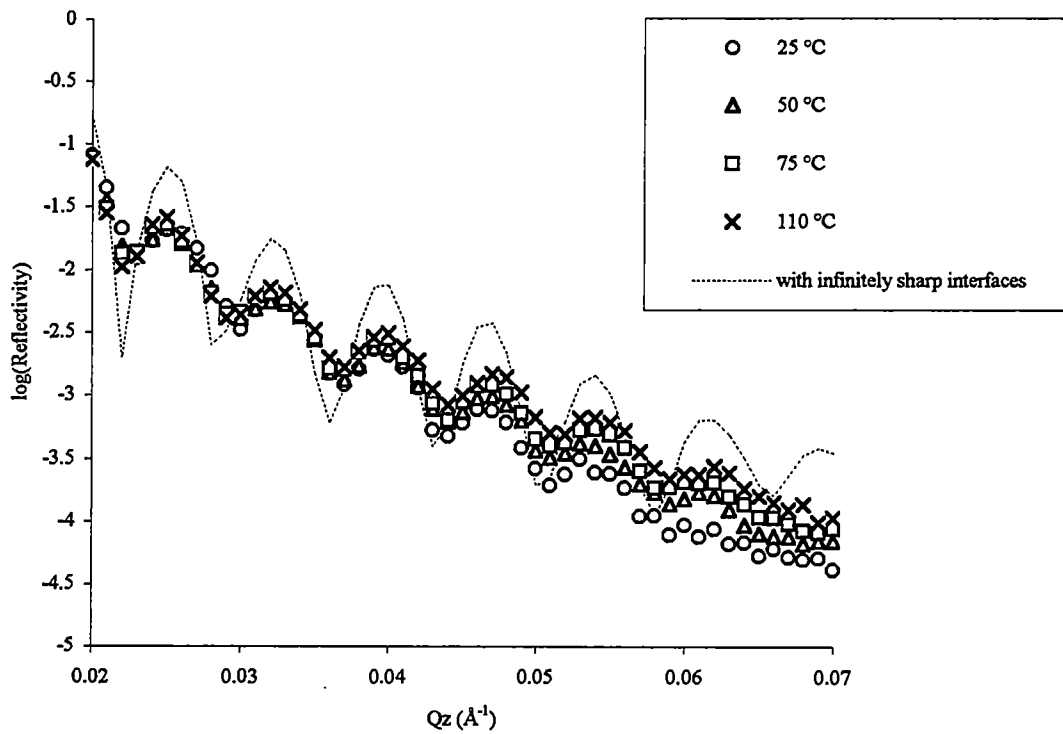


Figure 3.4. Magnified view of region $0.02 \leq Q_z \leq 0.07$

thickness of the *d*-PMMA. The interference fringes at higher Q_z dampen out due to the surface and/or interface roughness. With increasing temperature, these interference fringes dampen out more rapidly at higher Q_z . This may be due to the fact that the interfaces are broadening with increasing temperature. This aspect of the curve is difficult to discern visually, however any changes will be extracted from the curves through the fitting procedure. If the interfaces between the layers were infinitely sharp, the reflectivity curve would follow Porod's Law and decay as Q_z^{-4} [78]. Figure 3.3 also shows a calculated reflectivity profile for our system with infinitely sharp interfaces and surface (dashed curve). The expected location of a line with Q_z^{-4} dependence would pass through the center of the dashed curve. However, as can be seen from the comparison of the dashed curve and the experimental data (Figure 3.3), this is not the case for these samples. The curves all fall off more gradually than the dashed curve, signifying that the interfaces in the sample are not sharp and that there exists a gradient in the scattering length densities between layers. This gradient can be thought of as the transition zone width or roughness between consecutive layers. Thus, this transition zone width between the liquid crystal layer and the *d*-PMMA is the parameter that we are most interested in.

To quantitatively account for the descriptions portrayed in the above paragraph, a model fit was determined for each of the curves in Figure 3.3. Figure 3.5 shows the model fit and the measured reflectivity curve for the sample at 25 °C. The error bars on the experimental data correspond to the standard uncertainty in the measurement. Table 3.1 shows the result of this fitting procedure for the sample at 25 °C. This fit shows that the total thickness for the 8CB thin film is $1023 \pm 1 \text{ \AA}$. Included in this total thickness are

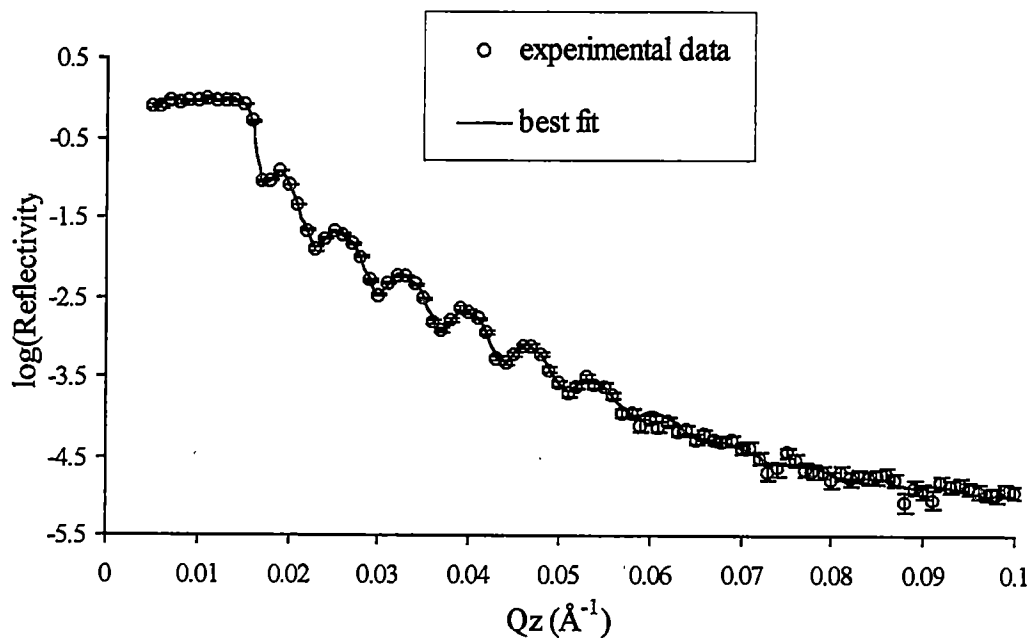


Figure 3.5. Neutron reflectivity data and best fit for the system at 25 °C

Table 3.1. Results from the fitted model to the experimental data for the sample at 25 °C

	(thickness \pm 1) Å	(roughness \pm 1) Å
aligned 8CB layer	110	5
bulk 8CB layer	631	5
8CB/ <i>d</i> -PMMA interface layer	282	328
<i>d</i> -PMMA	785	270
aluminum metal	869	29
aluminum oxide	88	61

three distinct scattering length density layers, which can be attributed to a layer that is ordered by the silicon surface, a bulk liquid crystal layer, and a layer that is influenced by the *d*-PMMA interface. The table also shows the thickness and transition zone widths (roughness) of the respective layers. The roughness reported in this table corresponds to that of the previous layer. For example, the roughness of the aligned 8CB layer (5 Å) corresponds to the silicon/aligned 8CB layer interface.

The data in Table 3.1 are displayed diagrammatically in Figure 3.6, which shows the scattering length density profile of the sample at 25 °C as a function of the layer depth (z) as determined from the fit. As was mentioned earlier, z is normal to the sample surface. Starting at the silicon substrate, one can see an aligned 8CB layer followed by the bulk 8CB layer and then the 8CB/*d*-PMMA interfacial layer. Inspection of this part of the figure can provide some interesting information. The scattering length density of the aligned layer near the silicon surface has a greater scattering length density than the bulk layer. This makes sense as the molecules in the ordered layer will be more efficiently packed, producing a system where there are more scattering centers per unit volume, which in turn results in a higher scattering length density.

Interestingly, inspection of Figure 3.6 can lead to the conclusion that there exists a broad interface between the bulk 8CB layer and the *d*-PMMA layer. However, fitting the experimental data to a multilayer system that has a broad interface between the bulk 8CB and the *d*-PMMA is not sufficient. A suitable fit can only be found if there exists a separate layer between the bulk 8CB and the *d*-PMMA layer. This result shows that there is a distinct scattering length density layer between the bulk 8CB and the *d*-PMMA layers, and not just a gradient in the density between the bulk 8CB and the *d*-PMMA.

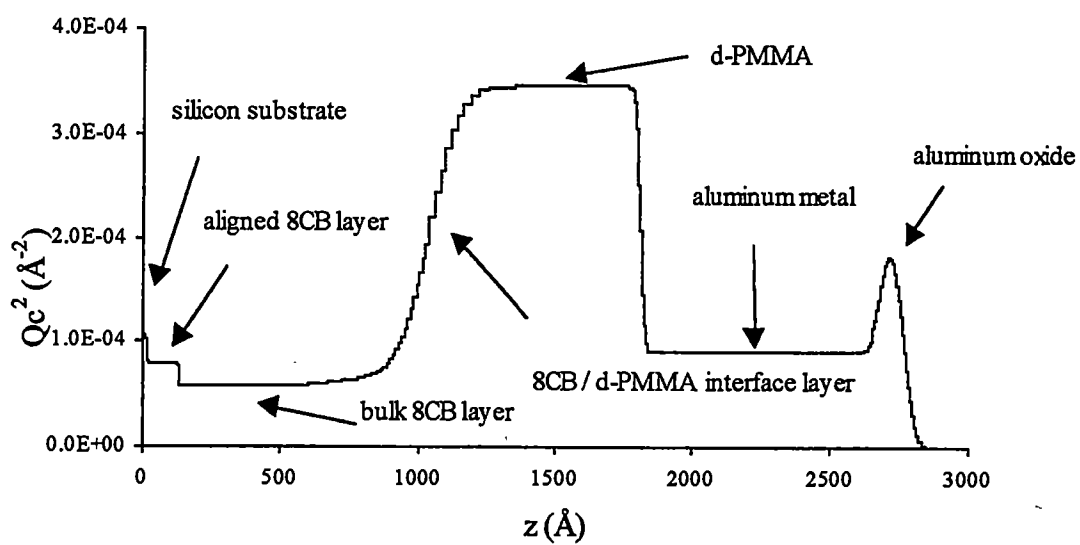


Figure 3.6. Relative scattering length density as a function of the layer depth (z) for the sample at 25 °C

Additionally, of the three layers within the 8CB thin film, this 8CB/*d*-PMMA interface layer has a higher scattering length density than the aligned and bulk 8CB layers. There are a number of possible interpretations of this fact. One is that it is a very well aligned layer of 8CB. The Q_c^2 of this layer is $1.34 \times 10^{-4} \text{ \AA}^{-2}$, as calculated from the model fit of the reflectivity profile. As the Q_c^2 is equal to $16\pi N_A \rho b / M$, the density or neutron scattering length of the layer can be determined from this data. Remember, N_A is the Avogadro constant, ρ is the mass density of the species, b is the neutron scattering length and M is the molecular weight of the species. If this layer were pure 8CB, the Q_c^2 value would translate to a mass density of 2.32 g/cm^3 . This value is much greater than the mass density of 8CB in the smectic-A phase, at $27.5 \text{ }^\circ\text{C}$, which is 1.03 g/cm^3 [79]. Therefore, this interpretation is not possible, as it would result in a layer that is denser than the bulk 8CB in the crystalline phase. Another possible explanation is that this separate layer is a narrow slice of a one-phase mixture of 8CB and *d*-PMMA. If this is indeed the case, the composition of this layer can be calculated from:

$$Q_c^2 (\text{layer}) = x_1 [Q_c^2 (8\text{CB})] + x_2 [Q_c^2 (d\text{-PMMA})]$$

$$x_1 + x_2 = 1$$

where x_1 is the mole fraction of 8CB, x_2 is the mole fraction of *d*-PMMA, $Q_c^2 (8\text{CB})$ is the scattering length density of the bulk 8CB, and $Q_c^2 (d\text{-PMMA})$ is the scattering length density of the *d*-PMMA. Using $Q_c^2 (\text{layer}) = 1.34 \times 10^{-4} \text{ \AA}^{-2}$, $Q_c^2 (8\text{CB}) = 9.67 \times 10^{-5} \text{ \AA}^{-2}$, and $Q_c^2 (d\text{-PMMA}) = 3.37 \times 10^{-4} \text{ \AA}^{-2}$, the composition of this interface layer is approximately 84% 8CB and 16% *d*-PMMA at all temperatures studied. However, inspection of the bulk phase diagram (Figure 3.7) shows that a mixture that is 84% 8CB and 16% *d*-PMMA will be phase separated for all of the temperatures below *ca* $90 \text{ }^\circ\text{C}$.

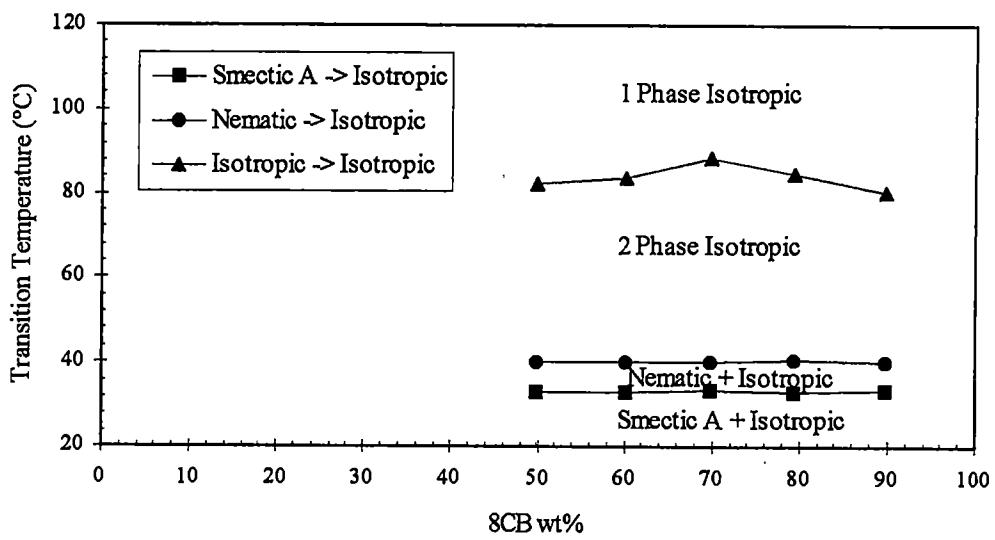


Figure 3.7. Bulk 8CB/PMMA phase diagram as determined by optical microscopy

Therefore, at this time, we are not able to accurately define the physical origin of this interfacial layer. It may be a mixture of an ordered 8CB with *d*-PMMA, though we are unable to definitively verify this. The origin of this interfacial layer could also be a consequence of the mathematical fitting procedure. An error function was used as the functional form to fit the interface. It is possible that there exists a different functional form that would describe the interface adequately without the interfacial layer. However, even without the interfacial layer, the fact remains that the interface is still quite broad.

The data shown in Figures 3.5 and 3.6 and Table 3.1 are for the sample at 25 °C. The same model must be utilized to fit the reflectivity data at the other temperatures also. Thus, the effect of thermal cycling on the 8CB/*d*-PMMA interface can also be evaluated from the results of these fits. Figure 3.8 is a plot that shows the temperature dependence of the thickness of the 8CB/*d*-PMMA interfacial layer as well as of the roughness between this layer and the *d*-PMMA. This figure demonstrates that the interfacial layer is between 250 and 300 Å and decreases slightly with temperature, while the roughness between the 8CB rich interfacial layer and the pure *d*-PMMA decreases from 270 Å at 25 °C down to 180 Å at 110 °C. Figure 3.8 also shows how the roughness between the bulk 8CB and the interfacial layers varies with increasing temperature. The roughness increases from 325 Å at 25 °C to 474 Å at 110 °C.

An aim of this experiment is to quantify the width of the interface between the 8CB and the polymer *d*-PMMA. Given the results described above, there are a number of ways to 'define' this interface. It could be the breadth of the sample between the bulk

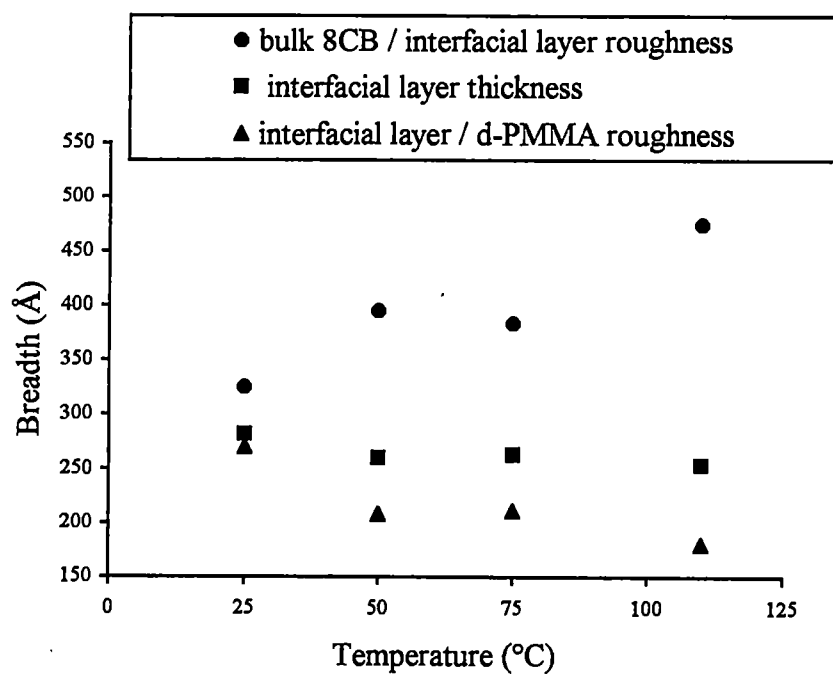


Figure 3.8. Breadth of the 8CB/*d*-PMMA interface as a function of temperature

8CB and the pure *d*-PMMA layer. If this definition is taken, the interface is on the order of 900 Å and changes only slightly with temperature. If however, the interfacial width is merely the roughness between the 8CB rich interfacial layer and the pure *d*-PMMA Figure 3.8 shows that this roughness is approximately 300 Å and decreases with temperature. In either definition, it can be stated that the interfacial width between a small molecule liquid crystal and *d*-PMMA is not sharp.

With this information regarding the temperature dependence of the 8CB/*d*-PMMA interface in a thin film, it is interesting to relate this to the phase behavior of the 8CB and PMMA in the bulk. From a theoretical standpoint, one would expect that the temperature dependence of the interface between two layers would depend on the miscibility of the two components that make up the layers. If the two components are miscible in the temperature range of interest, one would expect that an increase in temperature would increase the mobility of the two components and the interface would become broader, until the two layers mix to form one miscible system. On the other hand, if the two components are immiscible in the temperature range, one would expect that the interface would become broader with an decrease in $\Delta H/kT$ of the system, where ΔH is the enthalpy of mixing the two components, k is Boltzmann's constant, and T is the absolute temperature. This decrease in $\Delta H/kT$ correlates to an increase in temperature for a system with a lower critical solution temperature (LCST). Indeed studies of the phase behavior of cyanobiphenyls with poly(methyl methacrylate) or polystyrene [80-83] show phase diagrams that exhibit LCST behavior. Thus, the increase in the overall breadth of the LC/PMMA interface with an increase in temperature is understandable merely from the thermodynamics of the mixing process at the 8CB/*d*-PMMA interface.

However, a more careful inspection of the phase behavior of 8CB and PMMA elucidates a surprising effect: the 8CB and PMMA are miscible above approximately 80-90 °C. The phase diagram of 8CB and PMMA ($M_w = 120,000$) as determined by DSC and phase contrast microscopy in our lab is shown in Figure 3.7. Clearly, when the multilayer system is brought to 110 °C, the bulk system (regardless of composition) is in the miscible region. Therefore, one would expect that the multilayer system would mix to form a single layer of 8CB and *d*-PMMA at 110 °C. However, this is not what is found experimentally.

If the 8CB/*d*-PMMA bulk system was quenched from the one-phase region into the unstable part of the miscibility gap, phase separation by spontaneous amplification of concentration fluctuations would occur, *i.e.*, spinodal decomposition. The growth of 8CB rich and *d*-PMMA rich domains would be distinctly modified if the mixture was confined in a thin film geometry between planar parallel walls [85] due to specific preferred interactions between the walls and the mixed components. The preferred interaction of either component with a surface can result in the formation of a layered structure parallel to the walls.

The specific structure of the layered system will depend on the specific nature of the interactions between the walls and the thin films. Figures 3.9-3.13 show five possible equilibrium thin film structures for our system. In Figure 3.9, if there is no preferential interaction between the mixed components and the walls, the *d*-PMMA and 8CB will form a single phase thin film. Based on the experimental observations, this is not the case for the 8CB *d*-PMMA system. The reflectivity data simply cannot be fit to a single

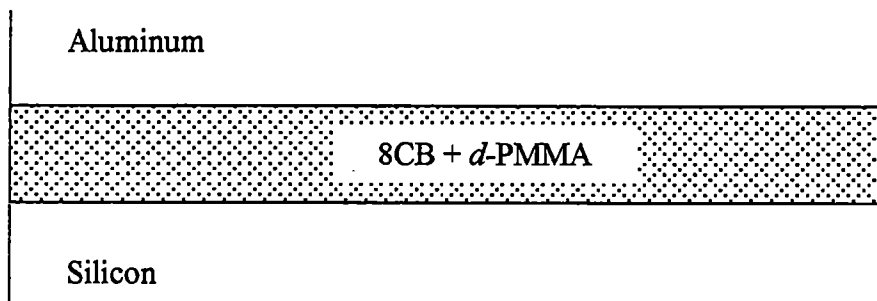


Figure 3.9. 8CB and *d*-PMMA are completely miscible to form a single phase

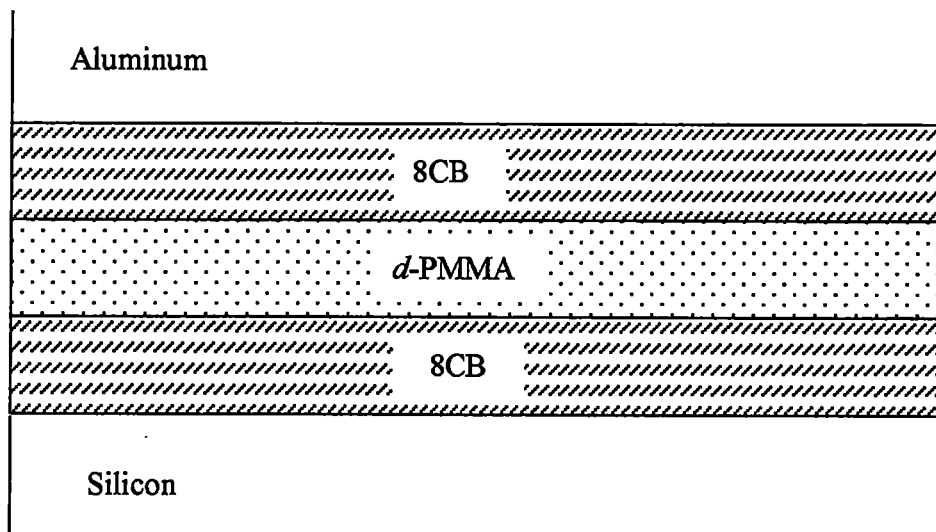


Figure 3.10. 8CB is energetically preferred by both the aluminum and silicon surfaces

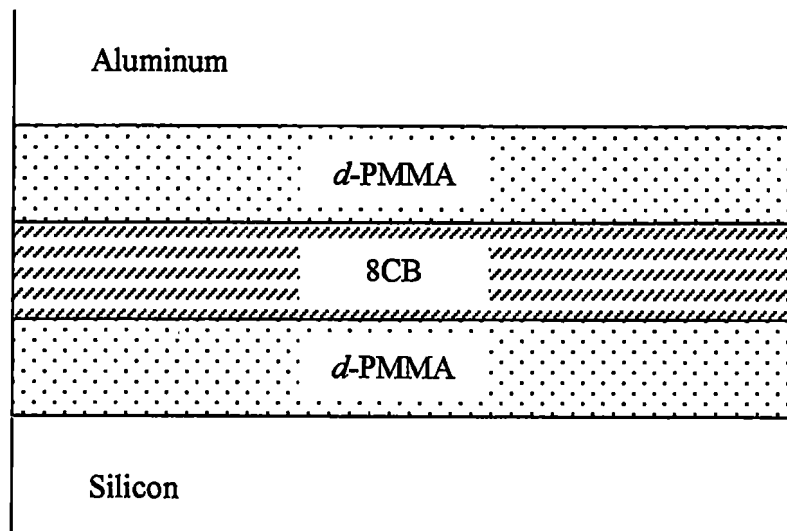


Figure 3.11. *d*-PMMA is energetically preferred by both the aluminum and silicon surfaces

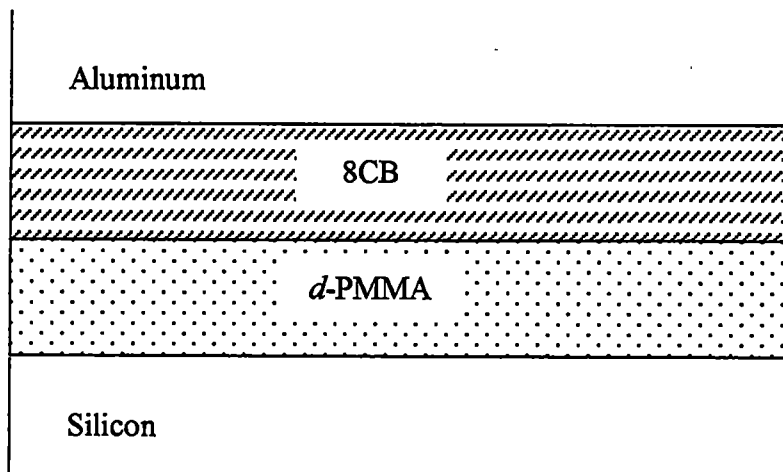


Figure 3.12. 8CB prefers aluminum surface only

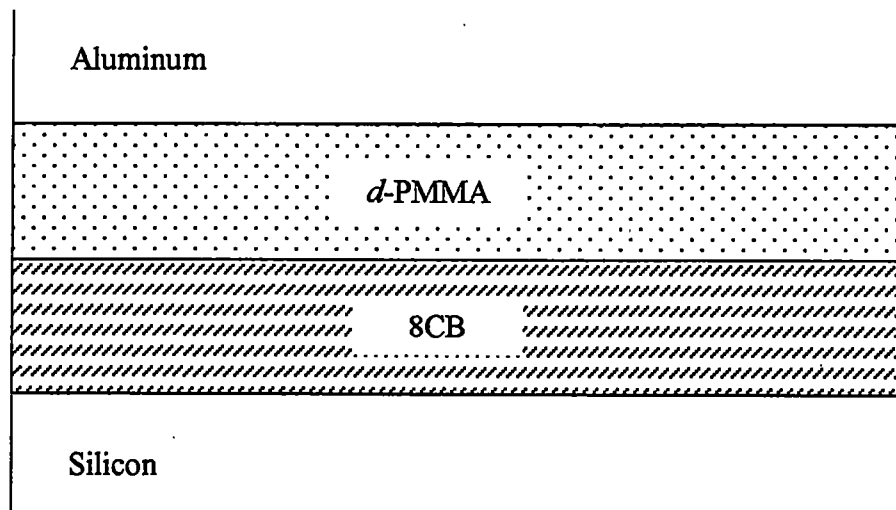


Figure 3.13. *d*-PMMA prefers aluminum surface only

layer between the aluminum and silicon substrate. Figure 3.10 depicts the situation where the 8CB is energetically preferred by both the aluminum and silicon surfaces. To test this, the contact angles of 8CB on a silicon oxide surface and an aluminum surface were measured. It was found that the contact angle of 8CB on silicon oxide is $(68.4 \pm 2.3)^\circ$ while its contact angle on aluminum is $(63.3 \pm 2.7)^\circ$. The similarity of these contact angles suggests that 8CB has similar affinity for the aluminum or silicon surface. However, fitting the reflectivity data assuming a layer of 8CB exists between the aluminum and *d*-PMMA was unsuccessful. Thus this picture does not depict the equilibrium structure of the 8CB and *d*-PMMA system. If the *d*-PMMA is energetically preferred by both the aluminum and silicon surfaces, then the resulting equilibrium structure should look something like Figure 3.11. Rulison calculated a surface energy of 0.038 J/m^2 for PMMA by measuring contact angles of various polar and nonpolar liquids on PMMA and using an Owens/Wendt plot [86]. Bikerman calculated the surface energy of aluminum to be 0.56 J/m^2 while Brunauer *et al.* calculated a surface energy of 0.42 J/m^2 for a silicon oxide surface [87,88]. Based on the surface energies of aluminum and silicon oxide relative to that of PMMA, the PMMA should have similar affinity to either the aluminum or silicon oxide surfaces. However, again the model fit to the reflectivity data precludes the existence of a film of *d*-PMMA at the silicon surface. The thin film equilibrium structure shown in Figure 3.12 can exist if the 8CB prefers the aluminum surface, or the *d*-PMMA prefers the silicon surface. The reflectivity results show, however, that no protonated material resides between the *d*-PMMA and aluminum. Lastly, Figure 3.13 shows the resulting equilibrium structure if *d*-PMMA prefers the

aluminum surface or 8CB prefers the silicon surface. Moreover, the thin film equilibrium structure of our system resembles that of Figure 3.13.

From the energetics of the contact angle and surface energy measurements, the *d*-PMMA and 8CB have similar affinity for both surfaces and thus one would predict that the resulting thin film structure should resemble Figures 3.10 or 3.11. Therefore why does the equilibrium thin film structure of the 8CB/*d*-PMMA system resemble Figure 3.13? Clearly the 8CB must prefer the silicon substrate, regardless of the contact angle measurements. This discrepancy can be understood when the anisotropy of the 8CB molecule is taken into consideration.

Much of the arguments that led to the development of the structures presented in Figures 3.10-3.13 assume the interaction between the thin film components and the surface are short-ranged, *i.e.*, do not extend beyond a monolayer. The influence of the surface on the structure of the thin film of 8CB clearly extends beyond a monolayer. The reflectivity results demonstrate that there exists a boundary layer of ordered liquid crystal that extends approximately 100 Å away from the surface. The existence of such an ordered layer is common in liquid crystals near a hard surface [90] and we propose that presence is responsible for the equilibrium thin film structure observed.

The presence of a surface in contact with a liquid crystal layer is known to induce an ordered boundary layer (see Figure 3.14) due to steric repulsions, van der Waals interactions and other couplings. The term "anchoring energy" is often introduced as the portion of the surface tension that is associated with the orientation of the liquid crystal at the surface that is different than the orientation of the liquid crystal in the bulk [89].

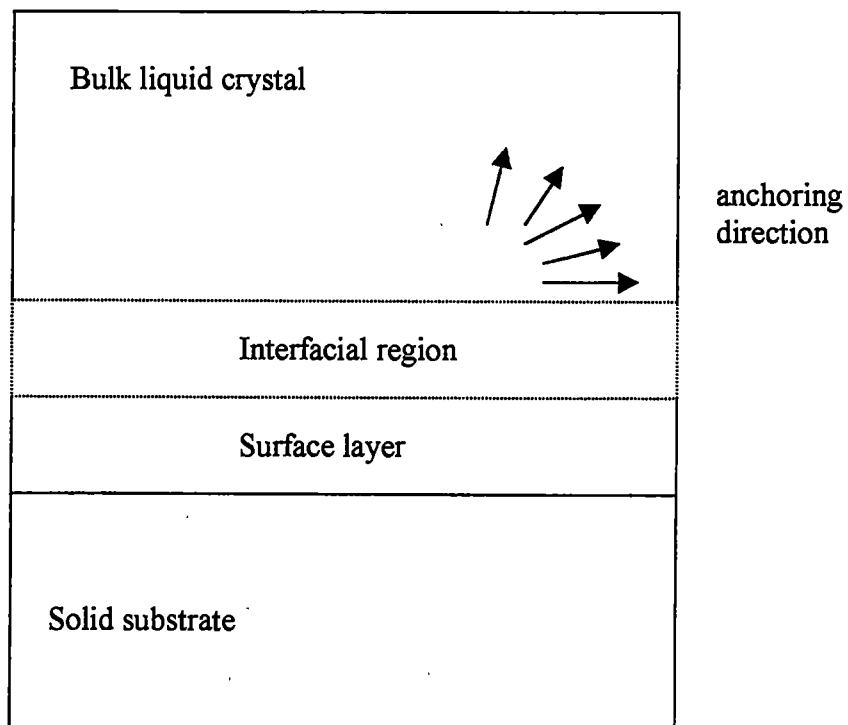


Figure 3.14. Schematic of a liquid crystal in contact with a solid substrate

Moreover, the presence of this orientational order at the surface or anchoring energy is known to impact the wetting behavior of a liquid crystal on a surface, often inducing a macroscopic layer of the nematic phase at the substrate. Essentially the presence of the surface induces order in the liquid crystal in proximity to the surface which alters the free energy of the system in the vicinity of the surface. This alteration in the free energy, in turn, often improves the wetting behavior of the liquid crystal on the surface.

Figures 3.9-3.13 have been described as due to the relative affinity of the thin film components for the surfaces. This behavior can also be described as due to the wetting behavior of the thin film components. In a thin film multicomponent system, there exists a competition between wetting and mixing. If mixing dominates over wetting, so that the 8CB and *d*-PMMA thin film system is a mixed single phase, then the resulting equilibrium structure would be that of Figure 3.9. If either component wets either or both surfaces as opposed to mixing, then a multilayered structure is observed (See Figures 3.10-3.13). If 8CB prefers, *i.e.*, wets both the aluminum and silicon surfaces as opposed to mixing, the thin film equilibrium structure resembles that of Figure 3.10. Likewise, the thin film equilibrium structure in Figure 3.11 results if *d*-PMMA wets both surfaces as opposed to mixing.

Therefore, it is the affinity of the liquid crystal for the surface that governs the wettability of the surface by the liquid crystal. This reasoning supports our conclusion that the presence of the oriented layer, and thus an anchoring energy, provides a physical description for the observed experimental system. Essentially, the anisotropy of the liquid crystal provides a mechanism for a "stronger" interaction between the liquid crystal

and the surface than would normally be found and this translates to an inhibition of the mixing behavior of our liquid crystal and polymer in a confined geometry.

Conclusion

Neutron reflectivity measurements have been completed to evaluate the breadth of the interface between a small molecule liquid crystal and a polymer. The results show that the liquid crystal layer consisting of 8CB that is situated between a silicon surface and a polymer, consists of three distinct scattering density layers. Furthermore, the interface between the liquid crystal and the interface is very broad, on the order of 300 – 900 Å. The interface also broadens with increasing temperature. One might expect the interfacial broadening to occur at elevated temperatures, but even at a lower temperature of 25 °C, this interface is still quite broad. This may have implications for current theories that implicitly treat the interface between a polymer and liquid crystal as a well-defined, sharp interface. It is the anchored layer of the 8CB which prohibits the complete miscibility of the 8CB and *d*-PMMA thin films. This anchored layer remains present, even at elevated temperatures.

References

- [1] Chadwick, J.; *Proceedings of the Royal Society (London)*; **A136**; p. 692; 1932
- [2] Bothe, W. and Becker, H.; *Naturwissenschaften*; **18**; p.705; 1930
- [3] Curie, I. and Joliot, F.; *Proceedings of the Royal Society*; **194**; p.273; 1932
- [4] Rutherford, E.; *Proceedings of the Royal Society (London)*; **A97**; p. 395; 1920
- [5] Dobrzynski, L. and Blinowski, K.; *Neutrons and Solid State Physics*; Ellis Horwood Limited; 1994
- [6] Opila, R.L.; Boerio, F.J.; Czanderna, A.W.; *Polymer/Inorganic Interfaces*; Materials Research Society, Pittsburgh; 1993
- [7] Sanchez, I.C.; *Physics of Polymer Surfaces and Interfaces*; Butterworth-Heinemann, Boston; 1992
- [8] Charmet, J.C. and de Gennes, P.G.; *Journal of the Optical Society of America*; **73**; p. 1777; 1983
- [9] Kim, M.W.; Pfeiffer, D.G.; Chen, W.; Hsiung, H.; Rasing, T.; Shen Y.R.; *Macromolecules*; **22**; p. 2682; 1989
- [10] Kim, M.W.; Liu, S.; Chang, T.C.; *Physical Review Letters*; **60**; p. 2745; 1988
- [11] Green, P.F.; Palmstrom, C.J.; Mayer, J.W.; Kramer, E.J.; *Macromolecules*; **18**; p. 501; 1985
- [12] Kramer, E.J.; Green, P.F.; Palmstrom, C.J.; *Polymer*; **25**; p. 473; 1984
- [13] Mills, P.J.; Green, P.F.; Palmstrom, C.J.; Mayer, J.W.; Kramer, E.J.; *Applied Physics Letters*; **53**; p. 2145; 1984
- [14] Green, P.F.; Mills, P.J.; Palmstrom, C.J.; Mayer, J.W.; Kramer, E.J.; *Materials Research Society Symposium Proceedings*; **40**; p.265; 1985

- [15] Kramer E.J.; Russell, T.P.; Volksen, W.; *Materials Research Society Symposium Proceedings*; **72**; p. 195; 1986
- [16] Coulon, G.; Russell, T.P.; Deline, V.R.; Green, P.F.; *Macromolecules*; **22**; p. 2581; 1989
- [17] Russell, T.P.; Coulon, G.; Deline, V.R.; Miller, D.C.; *Macromolecules*; **22**; p. 4600; 1989
- [18] Whitlow, S.J.; Wool, R.P.; *Macromolecules*; **22**; p. 2648; 1989
- [19] Brown, H.R.; Yang, A.C.M.; Russell, T.P.; Volksen, W.; Kramer, E.J.; *Polymer*; **29**; p. 1807; 1988
- [20] Hasegawa, H. and Hashimoto, T.; *Macromolecules*; **18**; p. 589; 1985
- [21] Henkee, C.S.; Thomas, E.L.; Fetters, L.J.; *Journal of Materials Science*; **23**; p. 1685; 1988
- [22] Thomas, H.R. and O'Malley, J.J.; *Macromolecules*; **12**; p.323; 1979
- [23] Schmitt, R.L.; Gardella, J.A.; Magill, J.H.; Salvati, L.; Chin, R.L.; *Macromolecules*; **18**; p. 2675; 1985
- [24] Bhatia, Q.S.; Pan, D.H.; Koberstein, J.T.; *Macromolecules*; **21**; p. 2166; 1988
- [25] Green, P.F.; Christensen, T.M.; Russell, T.P.; Jerome, R.; *Macromolecules*; **22**; p. 2189; 1989
- [26] Russell, T.P.; *Materials Science Reports*; **5**; p. 173; 1990
- [27] Stamm, M.; in [7]; p. 163
- [28] Stamm, M.; Huttenbach, S.; Reiter, G.; Springer, T.; *Europhysics Letters*; **14**; p. 451; 1991

- [29] Wu, W.L.; Orts, W.J.; Van Zanten, J.H.; Fanconi, B.M.; *Journal of Polymer Science: Part B: Polymer Physics*; **32**; p. 2475; 1994
- [30] Wallace, W.E.; Van Zanten, J.H.; Wu, W.L.; *Physical Review E*; **52**; p. R3329; 1995
- [31] Olbrich, E.; Marinov, O.; Davido, D.; *Physical Review E*; **48**; p. 2713; 1993
- [32] Marinov, O.; Olbrich, E.; Cohen, G.; Entin, I.; Davido, D.; *Physica A*; **200**; p.730; 1993
- [33] Phillips, P.L.; Richardson, R.M.; Zarbakhsh, A.; Haslam, S.D.; *Liquid Crystals*; **23**; p. 699; 1997
- [34] Cowie, J.M.G.; *Polymers: Chemistry & Physics of Modern Materials*; Chapman and Hall, New York; 1991
- [35] Niimura, N.; *Journal of Physics and Chemistry of Solids*; **60**; p.1265; 1999
- [36] Drake, J.M. and Klafter, J.; *Physics Today*; May; p. 46; 1990
- [37] Sun, S.F.; *Physical Chemistry of Macromolecules*; John Wiley & Sons Inc., New York, 1994
- [38] Leiser, G.; Fischer, E.W.; Ibel, K.; *Polymer Letters*; **13**; p. 39; 1975
- [39] Wignall, G.D.; Ballard, D.G.H.; Schelten, J.; *Journal of European Polymer J.*; **10**; p. 682; 1974
- [40] Kirste, R.G.; Kruse, W.A.; Ibel, K.; *Polymer*; **16**; p. 120; 1975
- [41] Cotton, J.P.; Decker, D.; Benoit, H.; Farnoux, B.; Higgins, J.; Jannick, G.; Ober, R.; Picot, C.; des Cloizeaux, J.; *Macromolecules*; **7**; p.963; 1974
- [42] Flory, P.J.; *Principles of Polymer Chemistry*; Cornell University Press, Ithaca, New York; 1967

- [43] Cotton, J.P.; Nierlich, M.; Boue, F.; Daoud, M.; Farnoux, B.; Jannink, G.; *Journal of Chemical Physics*; **65**; p. 1101; 1976
- [44] Wignall, G.D.; Farrar, N.R.; Morris, S.; *Journal of Materials Science*; **25**; p. 69; 1990
- [45] Rao, G.K.; *Multilevel Interconnect Technology*; McGraw-Hill, New York, 1993
- [46] Jin, C.; Luttmmer, J.D.; Smith, D.M.; Ramos, T.A.; *Materials Research Society Bulletin*; **22**; 10; p. 39; 1997
- [47] Hrubesh, L.W.; Keene, L.E.; Latorre, V.R.; *Journal of Materials Research*; **8**; p. 1736; 1993
- [48] Grasserbauer, M.; Werner, H.W.; *Analysis of Microelectronic Materials and Devices*; Wiley, New York; 1991
- [49] Petkov, M.P.; Weber, M.H.; Lynn, K.G.; Rodbell, K.P.; Cohen, S.A.; *Applied Physics Letters*; **74**; p. 2146; 1999
- [50] Gidley, D.W.; Frieze, W.E.; Dull, T.L.; Yee, A.F.; Ryan, E.T.; Ho, H.M.; *Physical Review B*; **60**; p. R5157; 1999
- [51] Petkov, M.P.; Weber, M.H.; Lynn, K.G.; Rodbell, K.P.; Cohen, S.A.; *Journal of Applied Physics*; **86**; p. 3104; 1999
- [52] Lekner, J.; *Theory of Reflection*; Nijhoff, Dordrecht; 1987
- [53] Dietrich, S.; Haase, A.; *Physical Review E*; **260**; p. 1; 1995
- [54] Chason, E.; Mayer, T.M.; *Critical Review of Solid State Materials Science*; **22**; p. 1; 1997
- [55] Higgins, J.S.; Benoit, H.C.; *Polymers and Neutron Scattering*; Oxford University Press, Oxford; 1994

- [56] Ramos, A.T.; Roderick, K.; Maskara, A.; Smith, D.; *Materials Research Society Symposium Proceedings*; **443**; p. 91; 1997
- [57] Jin, B.C.; List, S.; Yamanaka, S.; Lee, W.W.; Taylor, K.; Hsu, W.Y.; Olsen, L.; Luttmer, J.; Havemann, R.; *Materials Research Society Symposium Proceedings*; **443**; p. 99; 1997
- [58] Parratt, L.G.; *Review of Modern Physics*; **95**; p. 359; 1954
- [59] Ho, D.L.; Briber, R.M.; Jones, R.L.; Kumar, S.K.; Russell, T.P.; *Macromolecules*; **31**; p. 9247; 1998
- [60] Tesmer, J.R.; Nastasi, M.; *Handbook of Modern Ion Beam Materials Analysis*; Materials Research Society, Pittsburgh; 1995
- [61] Pan, Q.; Gonzales, G.B.; Composto, R.J.; Wallace, W.E.; Arkles, B.; Figge, L.K.; Berry, D.H.; *Thin Solid Films*; **345**; p. 244; 1999
- [62] Debye, P.; Anderson, H.R.; Brumberger, H.; *Journal of Applied Physics*; **28**; p. 679; 1957
- [63] Drzaic, P.S.; *Liquid Crystal Dispersions*; World Scientific Publishing Co. Pte. Ltd.; 1995
- [64] Crawford, G.P.; Zumer, S.; *Liquid Crystals in Complex Geometries Formed by Polymer and Porous Networks*; Taylor and Francis Ltd.; 1996
- [65] Hikmet, R.A.M.; Howard, R.; *Physical Review E*; **48**; p. 2752; 1993
- [66] Iannacchione, G.S.; Finotello, D.; *Physical Review Letters*; **69**; p. 2094; 1992
- [67] Bellini, T.; *et al.*; *Physical Review Letters*; **69**; p. 788; 1992
- [68] Clark, N.A.; *et al.*; *Physical Review Letters*; **71**; p. 3505; 1993
- [69] Iannacchione, G.S.; *et al.*; *Molecular Crystals and Liquid Crystals*; **262**; p. 13; 1995

- [70] Sinha, G.P.; Aliev, F.M.; *Physical Review E*; **58**; p. 2001; 1998
- [71] Dadmun, M.D.; Muthukumar, M.; *Journal of Chemical Physics*; **98**; p. 4850; 1993
- [72] Dadmun, M.D.; Muthukumar, M.; *Journal of Chemical Physics*; **101**; p. 10038; 1994
- [73] Yokoyama, H.; *Handbook of Liquid Crystal Research*; p. 179; Collings, P.J.; Patel, J.S. editors; Oxford University Press; 1997; And references therein
- [74] BDH: Product information; 1986
- [75] Certain commercial equipment, instruments, or materials are identified in this paper to adequately specify the experimental procedure. Such identification does not imply recommendation or endorsement by the National Institute of Standards and Technology, nor does it imply that the materials or equipment identified are necessarily the best available for the purpose.
- [76] Ankner, J.F.; Majkrzak, C.J.; *Neutron Optical Devices and Applications*; SPIE Proceedings **1738**; SPIE: Bellingham, WA; p. 260; 1992
- [77] Russell, T.P.; *Materials Science Reports*; **5**; p. 171; 1990
- [78] Porod, G.; *Kolloid-Z*; **124**; p. 83; 1951; **125**; p. 51; p. 109; 1952
- [79] Leadbetter, A.J.; Durrant, J.L.A.; Rugman, M.; *Molecular Crystals and Liquid Crystals*; **34**; p. 231; 1977
- [80] Ahn, W.; Kim, C.Y.; *Macromolecules*; **25**; p. 5002; 1992
- [81] Benmouna, F.; Daoudi, A.; Roussel, F.; Buisine, J.M.; Coqueret, X.; Maschke, U.; *Journal of polymer Science, Part B: Polymer Physics*; **37**; p. 1841; 1999
- [82] Benmouna, F.; Daoudi, A.; Roussel, F.; Leclercq, L.; Buisine, J.M.; Coqueret, X.; Benmouna, M.; Ewen, B.; Maschke, U.; *Macromolecules*; **33**; p. 960; 2000

- [83] Crawford, N.; Dadmun, M.D.; Unpublished Results
- [84] Born, M.; Wolf, E.; *Principles of Optics, 6th edition*; Pergamon Press, Oxford; 1980
- [85] Binder, K.; *Journal of Non-Equilibrium Thermodynamics*; **23**; p. 1; 1998
- [86] Rulison, C.; *ThetaDyne Corporation Scientific Instruments*; tutorial on solid surface energies; p. 11; 1998
- [87] Bikerman, J.J.; *Topics in Current Chemistry: Inorganic and Physical Chemistry*; Springer-Verlag, New York; p. 1; 1978
- [88] Brunauer, S.; Kantro, D.L.; Weise, C.H.; *Canadian Journal of Chemistry*; **37**; p. 714; 1959
- [89] Jerome, B.; in *Physical Properties of Liquid Crystals*; Wiley-VCH; p. 433; 1999
- [90] Lehmann, O.; *Handbuch der biologischen Arbeitsmethoden*; Urban and Schwarzenberg, Berlin; p. 123; 1922
- [91] Orts, W.J.; van Zanten, J.H.; Wu, W.; Satija, S.K.; *Physical Review Letters*; **71**; p. 867; 1993

Appendix

A.1

Small-Angle Neutron Scattering

In this section of the appendix, I will briefly describe the basics of neutron scattering and how the scattering intensity for the Debye density correlation function is derived. Coherent elastic scattering of neutrons measures the correlation between scattering centers within a medium providing information about the structural arrangement of the scattering centers. Expressions relating the scattering event to the scattering sample are expressed in terms of q . Scattering from a sample is shown in Figure A.1.1, where \mathbf{k}_i is the incident wave vector impinging on a point source and \mathbf{k}_f is the scattered wave vector. The magnitude of \mathbf{k}_i is $2\pi/\lambda$, which results from the geometry of Bragg diffraction. If the scattering is elastic, then the magnitude of \mathbf{k}_f is also equal to $2\pi/\lambda$. The resultant wave vector \mathbf{q} , is in the direction from the scattered beam to the incident beam so that $\mathbf{q} = \mathbf{k}_f - \mathbf{k}_i$ and θ is the scattering angle. For elastic scattering, $k_f = k_i$ and

$$|\mathbf{q}| = q = (4\pi/\lambda)\sin(\theta/2). \quad (\text{A.1.1})$$

Equation A.1.1 shows that q is dependent upon not only the angle of scatter measured, but also the wavelength.

In a neutron scattering experiment, one usually fixes the wavelength so that q depends upon the angle of the scattered wave. The incident flux (J_i) of neutrons is known and the scattered flux (J_f) of neutrons is measured at given angles. The differential scattering cross section $d\sigma/d\Omega$, is shown in Figure A.1.2 so that

$$d\sigma/d\Omega = J_f/J_i, \quad (\text{A.1.2})$$

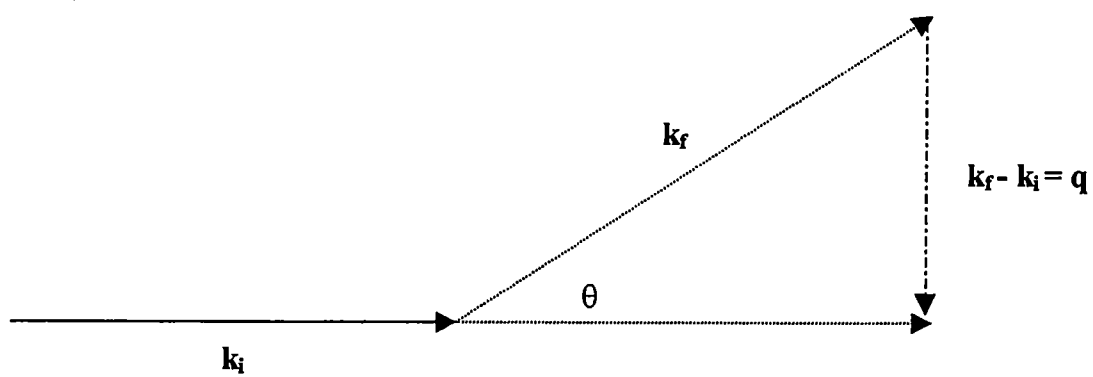


Figure A.1.1. Initial, scattered and resultant wave vectors

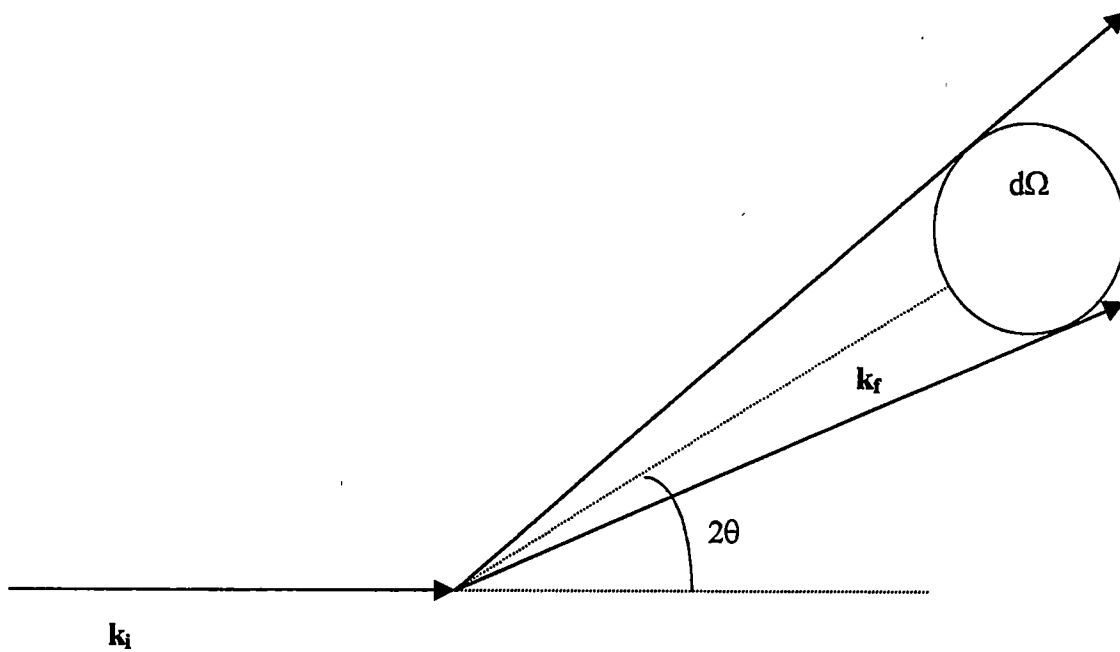


Figure A.1.2. Illustration of the differential scattering cross section

where J_f is the scattered flux of neutrons and J_i is the incident flux of neutrons. In words, the differential scattering cross section is equal to the number of particles scattered into a unit solid angle in a given direction per second, divided by the flux of the incident beam. The intensity (I) is simply the flux per unit solid angle.

The intensity of an electromagnetic wave is equal to the square of the amplitude (A) of a plane wave. The square of the amplitude is complex and $I = |A|^2 = AA^*$ where A^* is the complex conjugate of the amplitude. Since the intensity is a function of \mathbf{q} ($I(\mathbf{q})$), the amplitude is also a function of \mathbf{q} ($A(\mathbf{q})$). $A(\mathbf{q})$ is related to the scattering length density distribution of a species in real space by

$$A(\mathbf{q}) = \int_V \rho(\mathbf{r}) \exp(-i\mathbf{q}\mathbf{r}) d\mathbf{r}, \quad (\text{A.1.3})$$

where i is the square root of -1 , \exp is the exponential function and $\rho(\mathbf{r})$ is the scattering length density distribution in real space. The integrand is integrated over the sample volume illuminated by the incident neutron intensity. Thus, if $I(\mathbf{q}) = |A(\mathbf{q})|^2$, then

$$I(\mathbf{q}) = \left| \int_V \rho(\mathbf{r}) \exp(-i\mathbf{q}\mathbf{r}) d\mathbf{r} \right|^2. \quad (\text{A.1.4})$$

The scattered intensity $I(\mathbf{q})$ is the absolute square of the Fourier transform of the scattering length density distribution $\rho(\mathbf{r})$. When one measures $I(\mathbf{q})$, one is detecting the square of the amplitude of the signal. Since the signal is the Fourier transform of the scattering length density distribution of the sample, it would be convenient to take the inverse Fourier transform of the signal to get the scattering length density distribution

directly. However, since the signal is a square and complex, phase information of the wave is lost and one can not solve this analytically. One must assume a model, and fit the model to the measured data in order to glean any information. Given $I(\mathbf{q}) = A(\mathbf{q})A^*(\mathbf{q})$, if we let $\mathbf{r} = \mathbf{u}' - \mathbf{u}$, then

$$I(\mathbf{q}) = \left[\int_V \rho(\mathbf{u}') \exp(-i\mathbf{q}\mathbf{u}') d\mathbf{u}' \right] \left[\int_V \rho(\mathbf{u}) \exp(-i\mathbf{q}\mathbf{u}) d\mathbf{u} \right], \quad (\text{A.1.5})$$

or

$$I(\mathbf{q}) = \int_V \Gamma_\rho(\mathbf{r}) \exp(-i\mathbf{q}\mathbf{r}) d\mathbf{r}, \quad (\text{A.1.6})$$

where

$$\Gamma_\rho(\mathbf{r}) = \int_V \rho(\mathbf{u}) \rho(\mathbf{u} + \mathbf{r}) d\mathbf{u}. \quad (\text{A.1.7})$$

$\Gamma_\rho(\mathbf{r})$ in Equation A.1.7 is the auto-correlation function of the scattering length density distribution $\rho(\mathbf{r})$. The auto-correlation function specifies how the densities $\rho(\mathbf{u})$ and $\rho(\mathbf{u}')$ in neighboring regions separated by a distance \mathbf{r} , are correlated to each other, on the average. In order to detect any scattered intensity, there must exist a fluctuation in the scattering length density of the sample. Many other factors also contribute to the signal and must be taken into account. Factors such as the incoherent scattering from Hydrogen and spectrometer response must be carefully dealt with.

The thin films we studied are composed of nanopores connected by a pore wall material. The nanopores occupy much of the volume in the thin film. One can think of the film as a random two-phase structure. One phase is the voids or nanopores, with the pore wall material as the other phase. A suitable model to describe this random two-

phase structure was formulated by Debye [62]. Suppose one has an inhomogeneous solid with an average dielectric constant ϵ , and with local variations η . The variations η are described by a highly fluctuating function where the average value of η is zero. Within the solid, one picks two points η_1 and η_2 separated by a distance r . If one were to take the product of the two fluctuations $\eta_1\eta_2$, at different points throughout the solid keeping the distance r fixed, eventually an average of the product is obtained $\langle\eta_1\eta_2\rangle_{avg}$. For small distances $r = 0$ and $\langle\eta_1\eta_2\rangle_{avg} = \langle\eta^2\rangle$, while for large distances, $\langle\eta_1\eta_2\rangle_{avg} = 0$ because η_1 and η_2 will vary independently of one another. The average product of the fluctuations must be equal to some function multiplied by the mean square of the fluctuations, $\langle\eta^2\rangle$. This product is given as

$$\langle\eta_1\eta_2\rangle_{avg} = \gamma(r)\langle\eta^2\rangle. \quad (\text{A.1.8})$$

$\gamma(r)$ is known as the correlation function and has no physical dimensions. It is a number that varies with the distance r . Debye *et al.* go on to show that for a random two-phase structure

$$\gamma(r) = \exp(-r/\xi), \quad (\text{A.1.9})$$

where ξ is the characteristic correlation length. What Equation A.1.9 shows is that the probability of encountering two points with the same density separated by a distance r decays exponentially. To utilize this density correlation function to analyze the experimentally determined scattering intensity, its Fourier transform must be determined.

As was discussed earlier, the scattering intensity for a system is characterized by its scattering length distribution, $\rho(\mathbf{r})$, and is given by Equation A.1.6. The deviation $\eta(\mathbf{r})$ of the scattering length density distribution $\rho(\mathbf{r})$ from its mean is

$$\eta(\mathbf{r}) = \rho(\mathbf{r}) + \langle \rho \rangle. \quad (\text{A.1.10})$$

Thus the scattering intensity can be rewritten as

$$I(\mathbf{q}) = \int_v \Gamma_\eta(\mathbf{r}) \exp(-i\mathbf{q}\mathbf{r}) d\mathbf{r}, \quad (\text{A.1.11})$$

where $\Gamma_\eta(\mathbf{r})$ is the auto-correlation function of $\eta(\mathbf{r})$. Substituting the Debye density correlation function, $\gamma(r) = \exp(-r/\xi)$, for the auto-correlation function, $\Gamma_\eta(\mathbf{r})$, one obtains

$$I(\mathbf{q}) = \langle \eta^2 \rangle V \int_v \gamma(r) \exp(-i\mathbf{q}\mathbf{r}) d\mathbf{r}, \quad (\text{A.1.12})$$

where V is the volume and $\langle \eta^2 \rangle$ is the mean square of the fluctuations. The term $\langle \eta^2 \rangle V$ is a normalization factor in going from the auto-correlation function, $\Gamma_\eta(\mathbf{r})$, to the Debye density correlation function, $\gamma(r)$.

The quantity that represents the total scattering power of the sample is the invariant Q . It is evaluated by integrating the observed intensity, $I(\mathbf{q})$, over the whole reciprocal space. For an isotropic material, the invariant is

$$Q = (1/2\pi^2) \int_0^\infty q^2 I(q) dq. \quad (\text{A.1.13})$$

If the volume fractions of an ideal two phase system are ϕ_1 and ϕ_2 , then $1 = \phi_1 + \phi_2$.

The average scattering length density is for a two phase system is

$$\langle \rho \rangle = \phi_1 \rho_1 + \phi_2 \rho_2, \quad (\text{A.1.14})$$

where the fluctuations of the two different phases are defined as

$$\eta_1 = \rho_1 - \langle \rho \rangle = \Delta\rho\phi_2 \quad \text{and} \quad \eta_2 = \rho_2 - \langle \rho \rangle = -\Delta\rho\phi_1, \quad (\text{A.1.15})$$

where

$$\Delta\rho = \rho_1 - \rho_2 = \eta_1 - \eta_2. \quad (\text{A.1.16})$$

The invariant, Q , equates to

$$Q = V\langle\eta^2\rangle = V(\eta_1^2\phi_1 + \eta_2^2\phi_2) = V(\Delta\rho)^2\phi_1\phi_2. \quad (\text{A.1.17})$$

If the observed scattering intensity $I(\mathbf{q})$ is integrated over the whole reciprocal space, the invariant Q is found to be related to the total volume of the sample, the difference in the scattering length densities and volume fractions of the two phases. Substituting

$V(\Delta\rho)^2\phi_1\phi_2$ for $V\langle\eta^2\rangle$ in Equation A.1.12, we get

$$I(\mathbf{q}) = V(\Delta\rho)^2\phi_1\phi_2 \int_v \gamma(\mathbf{r}) \exp(-i\mathbf{q}\mathbf{r}) d\mathbf{r}. \quad (\text{A.1.18})$$

The next step is to solve the integral of

$$\int_v \gamma(\mathbf{r}) \exp(-i\mathbf{q}\mathbf{r}) d\mathbf{r}. \quad (\text{A.1.19})$$

Since we are integrating over a volume,

$$\int_v \gamma(\mathbf{r}) \exp(-i\mathbf{q}\mathbf{r}) d\mathbf{r} = \int \gamma(\mathbf{r}) \exp(-i\mathbf{q}\mathbf{r}) d^3\mathbf{r}. \quad (\text{A.1.20})$$

In spherical coordinates, $d^3\mathbf{r} = dV = (r\sin\theta d\theta)(r d\phi)(dr) = r^2 \sin\theta d\theta d\phi dr$, and since the system has spherical symmetry, $\mathbf{q}\mathbf{r} = qr(\cos\theta)$. Using these relations, Equation A.1.20 becomes

$$\int_0^\infty \gamma(r) \int_0^\pi \exp(iqr\cos\theta) \sin\theta d\theta r^2 dr \int_0^{2\pi} d\phi. \quad (\text{A.1.21})$$

$$\int_0^{2\pi} d\phi \int_0^\pi \exp(iqr\cos\theta) \sin\theta d\theta r^2 dr = 2\pi [4\sin(qr)/qr] r^2 dr$$

$$(A.1.22)$$

so that the scattering intensity is

$$(A.1.23)$$

$$I(q) = 8\pi(\Delta\rho)^2 \phi_1\phi_2 \int_0^{\infty} \gamma(r) [\sin(qr)/qr] r^2 dr.$$

From Equation A.1.9, $\gamma(r) = \exp(-r/\xi)$, the expression for the scattering intensity $I(q)$ is

$$I(q) = 8\pi(\Delta\rho)^2 \phi_1\phi_2 \int_0^{\infty} \exp(-r/\xi) [\sin(qr)/qr] r^2 dr. \quad (A.1.24)$$

Let $u = qr$ and $b = 1/q\xi$, and $dr = du/q$,

$$I(q) = 8\pi(\Delta\rho)^2 \phi_1\phi_2 \int_0^{\infty} \exp(-bu) [\sin(u)/u] (u/q)^2 (du/q).$$

$$(A.1.25)$$

Since the integration is with respect to u , and $\sin(u) = [\exp(iu) - \exp(-iu)]/2i$, then

Equation A.1.25 is

$$I(q) = 8\pi(\Delta\rho)^2 \phi_1\phi_2 / q^3 \int_0^{\infty} \exp(-bu) [\sin(u)] u du$$

$$(A.1.26)$$

Let $\sin(u) = [\exp(iu) - \exp(-iu)]/2i$, then

$$I(q) = 8\pi(\Delta\rho)^2 \phi_1\phi_2 / 2iq^3 \int_0^{\infty} u \{ \exp[(-u)(b-i)] - \exp[(-u)(b+i)] \} du.$$

$$(A.1.27)$$

The solution of the integral of $u \exp[-(u)(a)]du$ is equal to $1/a^2$. The solution to our integral is $[1/(b-i)^2] - [1/(b+i)^2]$, which gives the scattering intensity as

$$I(\mathbf{q}) = \{8\pi(\Delta\rho)^2\phi_1\phi_2/2iq^3\} \{[1/(b-i)^2] - [1/(b+i)^2]\}. \quad (\text{A.1.28})$$

Simplifying Equation A.1.28, one gets

$$I(\mathbf{q}) = \{8\pi(\Delta\rho)^2\phi_1\phi_2/2iq^3\} \{2ib/(b+i)^2\}, \quad (\text{A.1.29})$$

and substituting back in $b = 1/q\xi$,

$$I(\mathbf{q}) = 8\pi(\Delta\rho)^2\phi_1\phi_2[\xi^3/(1+q^2\xi^2)^2]. \quad (\text{A.1.30})$$

Equation A.1.30 is the SANS intensity based on the Debye density correlation function for a random two-phase system. For our system consisting of pores, P, and pore wall material, (1 - P), if $\phi_1 = P$ and $\phi_2 = (1 - P)$, then

$$I(\mathbf{q}) = 8\pi(\Delta\rho)^2P(1-P)[\xi^3/(1+q^2\xi^2)^2]. \quad (\text{A.1.31})$$

A.2

Neutron Reflectivity

The following discussion pertains to neutron reflectivity that is utilized in the experiments described in section 3.2. However, the same equations that will be used in this discussion can also be applied for x-rays and thus pertinent to the x-ray reflectivity in section 2.2 of this thesis.

Any radiation incident on an interface can refract or reflect as long as the refractive indices on both sides of the interface are different. The interface can be between two different materials or between the surface of a medium and air or vacuum. In general, the refractive index of a medium, n , is complex and given by

$$n = 1 - \delta + i\beta. \quad [84] \quad (\text{A.2.1})$$

For polymers, the refractive index is usually slightly less than unity [77]. The imaginary component of the refractive index $i\beta$, takes into account that the medium may absorb the radiation. In most cases, the absorption factor for neutrons is so small that this term can be neglected. If the absorption factor for neutrons is zero, $\beta_N \approx 0$, then $n = 1 - \delta_N$. The real component of the refractive index for neutrons is

$$\delta_N = (\lambda^2/2\pi)N_A[\Sigma_i(\rho_i b_i/A_i)], \quad (\text{A.2.2})$$

where λ is the wavelength of the incident neutrons, N_A is Avogadro's number. Within the summation Σ_i , b_i is the neutron scattering length for species i with density ρ_i and atomic weight A_i . In the case of polymers, this summation can be dealt with by using the monomer units since each monomer unit will have the same neutron scattering length and density. In this case the real component will be

$$\delta_N = (\lambda^2/2\pi)(N_A\rho)(b_{\text{mon}}/M_{\text{mon}}), \quad (\text{A.2.3})$$

where ρ is the mass density of the polymer, b_{mon} is the neutron scattering length and M_{mon} is the molecular weight of the monomer. The real component δ_N , is usually on the order of 10^{-6} and positive for most media. This implies that the refractive index n , will be slightly less than 1; 1 being the refractive index of air or vacuum.

Figure A.2.1 is a diagram that illustrates the relationship between reflected and refracted radiation. At an interface between two different media, the ratio of the refractive indices, n_1/n_2 , determines the angle at which the radiation is refracted. In Figure A.2.1, θ_1 is the grazing angle of incident radiation and θ_2 is the angle of refraction with respect to the surface plane. Snell's law describes this relationship and is given by

$$n_1 \cos(\theta_1) = n_2 \cos(\theta_2). \quad [84] \quad (\text{A.2.4})$$

If the interface is between a medium and air or vacuum, then $n_1 = 1$ and Snell's law is

$$\cos(\theta_2) = (1/n_2) \cos(\theta_1). \quad (\text{A.2.5})$$

If δ_N is less than 1, then n_2 is greater than 0 ($n = 1 - \delta_N$) and there exists a real angle of refraction, θ_2 , for all incident angles θ_1 . If δ_N is greater than 1, then n_2 is less than 0 and θ_2 is less than θ_1 . In this case, there is a real angle of refraction, θ_2 , for all incident angles, θ_1 , as long as θ_1 is greater than the critical angle, θ_c . The critical angle θ_c is defined as the angle below which total external reflection occurs. The angle of refraction, θ_2 , is 0 at

$$\cos(\theta_c) = \cos(\theta_1) = n_2. \quad (\text{A.2.6})$$

According to Snell's law, a good approximation of the critical angle, θ_c , is $(2\delta_N)^{1/2}$ [52].

From this relationship, one can see that the critical angle depends only on the wavelength

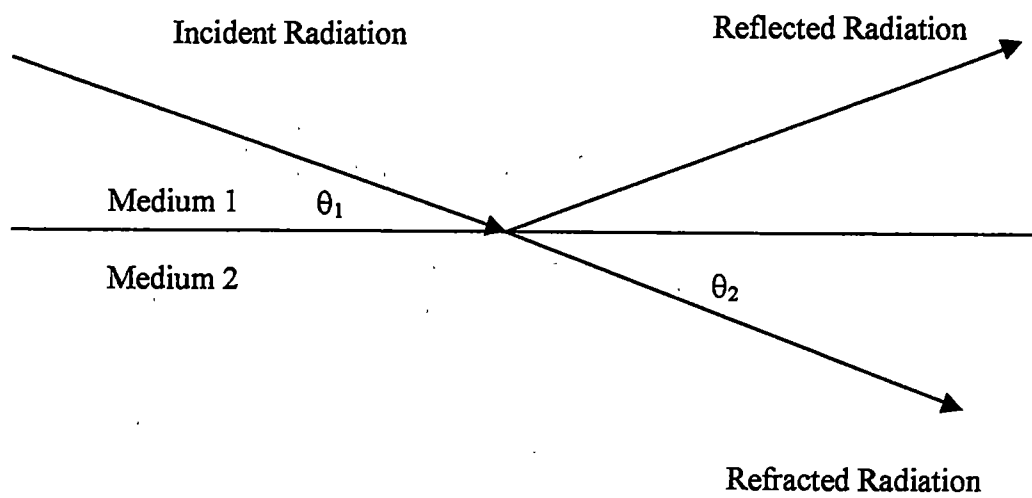


Figure A.2.1. Relationship between reflected and refracted radiation

of the incident neutrons and the neutron scattering length density of the medium ($\delta_N \approx [\lambda^2][\Sigma_i(\rho_i b_i/A_i)]$).

The momentum transfer in the z direction (normal to a surface) in a medium on either side of an interface determines the extent to which incident neutrons will be reflected.

The z component of this momentum transfer in a vacuum (0) is given by

$$k_{z,0} = (4\pi/\lambda) \sin(\theta). \quad [52] \quad (\text{A.2.7})$$

The grazing angle of incidence is θ where λ is the wavelength of incident neutrons.

Only the z component (normal to the surface) of the momentum transfer is applicable because specular conditions are assumed, i.e., the angle of incidence is equal to the angle of detection. Notice that the wave vector $k_{z,0}$ is similar to the wave vector in small-angle scattering ($q = (4\pi/\lambda) \sin(\theta/2)$). However, $k_{z,0}$ pertains only to the z component of the scattering, hence the distinction $k_{z,0}$ is made as opposed to q . For a medium i with a neutron scattering length density ρ_n , the z component of the momentum transfer is

$$k_{z,i} = \{[(4\pi/\lambda) \sin(\theta)]^2 - [4\pi\rho_n]\}^{1/2}. \quad (\text{A.2.8})$$

The first term is the z component of momentum transfer in a vacuum. This equation shows the relationship between the wave vector and the scattering length density of the species i . Furthermore, the quantity $[4\pi\rho_n]$ is equal to the square of the critical value of $k_{z,i}$ so that

$$k_{z,i} = [(k_{z,0})^2 - (k_{c,i})^2]^{1/2}. \quad (\text{A.2.9})$$

The critical value ($k_{c,i}$) is the value of $k_{z,i}$ below which total reflection occurs. From the critical value of the wave vector, one can obtain the mean scattering length density of a

species. In the discussions of x-ray and neutron reflectivity in sections 2.2 and 3.2, we are using Q_z to denote the z component of the wave vector. Q_z is related to $k_{z,i}$ by

$$Q_z = 4k_{z,i}^2. \quad (\text{A.2.10})$$

The Fresnel reflectivity, R_F , is the product of the reflection coefficient (r) and its complex conjugate ($R_F = rr^*$) [84]. The reflection coefficient at an infinitely sharp interface separating two media, i and $i + 1$, is

$$r_{i,i+1} = (k_{z,i} - k_{z,i+1}) / (k_{z,i} + k_{z,i+1}). \quad (\text{A.2.11})$$

For example, the reflectance coefficient for a vacuum (0) / metal (1) interface would be

$$r_{0,1} = (k_{z,0} - k_{z,1}) / (k_{z,0} + k_{z,1}). \quad (\text{A.2.12})$$

Using the relationship between the wave vector and its critical value, the reflectance coefficient for the interface described above is

$$r_{0,1} = \{k_{z,0} - [(k_{z,0})^2 - (k_{c,1})^2]^{1/2}\} / \{k_{z,0} + [(k_{z,0})^2 - (k_{c,1})^2]^{1/2}\}. \quad (\text{A.2.13})$$

Using this equation for the reflectance coefficient and multiplying it by its complex conjugate, one obtains

$$R_F(k_{z,0}) = | \{1 - [1 - (k_{c,1}/k_{z,0})^2]^{1/2}\} / \{1 + [1 - (k_{c,1}/k_{z,0})^2]^{1/2}\} |^2. \quad (\text{A.2.14})$$

This is the Fresnel reflectivity as a function of the z component of the wave vector for a vacuum (0) / specimen (1) interface. If $k_{z,0} \leq k_{c,1}$, total reflection occurs and the Fresnel reflectivity is unity. For values of $k_{z,0} > k_{c,1}$, R_F is proportional to $(k_{c,1}/k_{z,0})^4$. If the interface is infinitely sharp, the reflectivity will vary as $k_{z,0}^{-4}$ for $k_{z,0} > k_{c,1}$. If the interface is rough, the reflectivity will decay more rapidly than $k_{z,0}^{-4}$.

Figure A.2.2 is a diagram of a medium with thickness, d , on a substrate in a vacuum. The incident neutron beam impinges on the medium with a grazing angle θ_0 . The beam is reflected at an angle equal to θ_0 in order to satisfy the specular condition. θ_m is the

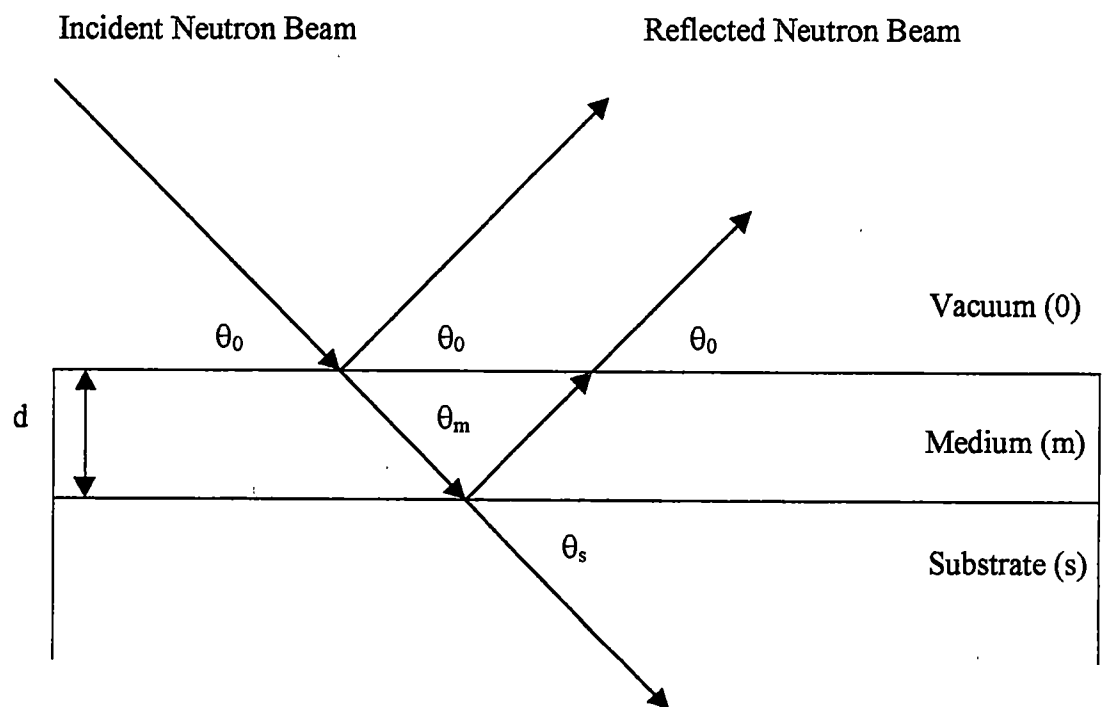


Figure A.2.2. Medium with thickness d , on a substrate

angle that the beam is refracted at the vacuum (0) / medium (m) interface. The beam is then reflected and refracted with an angle θ_s at the medium (m) / substrate (s) interface.

If we denote $r_{0,m}$ and $r_{m,s}$ as the reflectivity coefficients of the vacuum / medium and medium / substrate interfaces, the overall reflectivity coefficient is

$$r = \{r_{0,m} + [(r_{m,s})\exp(2ik_{z,m}d)]\} / \{1 + [(r_{0,m}r_{m,s})\exp(2ik_{z,m}d)]\}, \quad (\text{A.2.15})$$

where d is the thickness and $k_{z,m}$ is the momentum transfer within the medium, \exp is the exponential function and $i = (-1)^{1/2}$. The exact solution of the Fresnel reflectivity for this is system is

$$R_F(k_{z,0}) = r r^* = \{ |r_{0,m}|^2 + |r_{m,s}|^2 + 2[(r_{0,m}r_{m,s})\exp(2ik_{z,m}d)] / \{1 + |(r_{0,m}r_{m,s})|^2 + 2[(r_{0,m}r_{m,s})\exp(2ik_{z,m}d)]\}. \quad (\text{A.2.16})$$

If the reflectance's for the interfaces are real, then the above equation reduces to

$$R_F(k_{z,0}) = r r^* = \{ r_{0,m}^2 + r_{m,s}^2 + 2[(r_{0,m}r_{m,s})\cos(2k_{z,m}d)] / \{1 + (r_{0,m}r_{m,s})^2 + 2[(r_{0,m}r_{m,s})\cos(2k_{z,m}d)]\}. \quad (\text{A.2.17})$$

Figure A.2.3 is a typical reflectivity profile for a medium on a substrate. In this case the medium is a thin film of poly(methyl methacrylate) (PMMA) supported on a silicon substrate. In a specular reflectivity experiment, the Fresnel reflectivity, R_F , is measured as a function of the wave vector, Q_z , at grazing angles incident to the sample surface. R_F is simply the reflected intensity divided by the initial intensity, I/I_0 . In Figure A.2.3, the results are presented as the $\log(I/I_0)$ vs. Q_z . Figure A.2.3 also shows a series of maxima and minima. Differentiation of the cosine arguments ($2k_{z,m}d$) in the above equation shows that the minima result for even multiples of π . The thickness, d , of the sample can thus be calculated from the distance between two successive minima:

$$d = 2\pi / \Delta Q_z. \quad (\text{A.2.18})$$

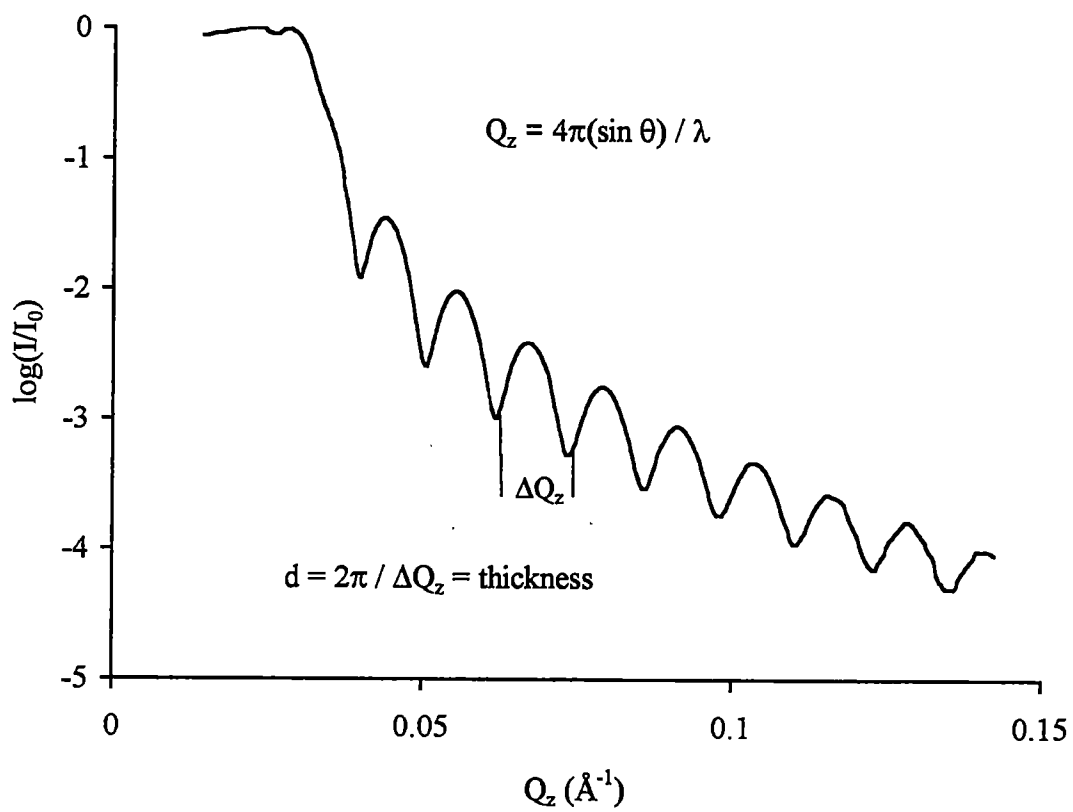


Figure A.2.3. Reflectivity profile of PMMA on a silicon substrate

For a multilayer system, the reflectivity can be calculated in a recursion manner. For example a sample that contains two layers on a substrate (s) with layer 1 in contact with a vacuum (0) and layer 2 in contact with the substrate. Starting with the bottom layer, the reflectance coefficient of layer 2 and the substrate is used to calculate the reflectivity for the layer 2 / substrate interface, $R_{2,s}$. The reflectance coefficient for layer 1 and layer 2 along with $R_{2,s}$ is used to calculate the reflectivity for the layer 1 / layer 2 interface, $R_{1,2}$. Finally, the vacuum / layer 1 interface reflectivity, $R_{0,1}$, is calculated from the reflectance coefficient for vacuum and layer 1 along with $R_{1,2}$. In a multilayer system, every interface and layer contributes to the reflectivity profile. The observed reflectivity profile for a multilayer sample is a convolution of all the reflectances from individual layers and interfaces.

So far we have discussed reflectivity at infinitely sharp interfaces. In the real world, this is usually not the case. There almost always exists a gradient in the density across an interface between consecutive layers, i.e. roughness. For most systems, the variation in scattering length density is continuous across an interface and not discrete.

Experimentally, one measures the reflectivity profile and tries to derive the variation in scattering length density. The intensity one measures is the Fourier transform of the variation in scattering length density. It would be nice to take the inverse Fourier transform of the intensity to retrieve the variations in scattering length density. However, like other scattering techniques, this is not possible. The intensity is the square of the reflection amplitudes and the phase information is lost upon using the inverse Fourier transform. A direct analytical solution is therefore not possible. A consequence of this is

that more than one scattering length density profile may yield the same measured reflectivity profile.

One way to solve the problem of analyzing a measured profile, is to assume a model and calculate the corresponding reflectivity profile. From the model, one can calculate the scattering length density profile, normal to the surface, as a function of depth. This concentration profile can be well approximated by subdividing the continuous function into a series of discrete steps. The smaller the steps to approximate the function, the better this approximation is. One can then vary the parameters of the model and obtain a best fit to the data. An iterative process can minimize discrepancies between the model and the measured data where the critical Q_z (Q_c), thickness and roughness of the individual layers are systematically varied.

We used the program mlayer to generate concentration profiles based on our model, and ultimately obtain the best fit to our measured reflectivity data. The program mlayer, developed by Ankner [76], uses an iterative algorithm to generate a series of concentration profiles based on the parameters Q_c , thickness, roughness and absorption coefficient of individual layers. It also takes into account the wavelength spread and angular resolution of the instrument. If the interfaces were perfectly sharp, the concentration profile as a function of depth, could be represented by a series of step functions,

$$\rho(z) = \rho_1 \Theta(z - z_0) + (\rho_s - \rho_1) \Theta(z - z_0 - d_1), \quad (\text{A.2.19})$$

where Θ is the Heaviside unit step function, ρ_1 and ρ_s are the scattering length densities for layer 1 and substrate respectively, d_1 is the thickness for layer 1, and z_0 is an arbitrary depth where the vacuum / layer 1 interface is placed. However, roughness can act to

smear a perfectly sharp interface, so that the concentration profile is more properly represented by

$$\rho(z) = \rho_1 \int_0^z dz' I(z-z', \sigma_{\text{vacuum/layer}}) \gamma(z'-z_0) + (\rho_s - \rho_1) \int_0^z dz' I(z-z', \sigma_{\text{layer/substrate}}) \gamma(z'-z_0 - d_1). \quad (\text{A.2.20})$$

The functions $I(z, \sigma)$ are convoluted with the scattering density steps and round off their sharp edges. The interfacial function that is often used is a Gaussian

$$I(z, \sigma) = [1/\sigma(2\pi)^{1/2}] [\exp(-z^2/2\sigma^2)], \quad (\text{A.2.21})$$

where σ is characteristic width of the interface (approximately equal to the half-width at half maximum). The convolution of a Gaussian with a unit step Θ yields an error function. The complete scattering density profile is generated by discretizing the error function as a series of small density increments, calculating the specular reflectivity, and varying the interfacial width parameters σ (roughness), layer thickness d , and scattering density Q_c using a non-linear least squares fit routine to minimize the chi-square distribution (χ^2).

Vita

Gary W. Lynn was born on October 27, 1971 in Topeka, Kansas. He received a B.S. degree in Chemistry from Washburn University in the spring of 1995. In the fall of 1995, he then started his pursuit of a Ph.D. degree in Chemistry at the University of Tennessee, Knoxville. He was fortunate enough to hold the position of Guest Researcher in the Polymers Division at the National Institute of Standards and Technology from the summer of 1998 through the fall of 1999.